Journal Pre-proof

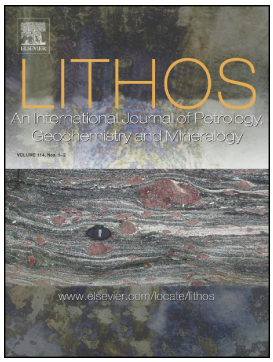

Linking magma texture, rheology and eruptive style during the 472 AD Pollena Subplinian eruption (Somma-Vesuvius)

Alessandro Vona, Claudia Romano, Guido Giordano, Roberto Sulpizio

PII: S0024-4937(20)30295-4

DOI: https://doi.org/10.1016/j.lithos.2020.105658

Reference: LITHOS 105658

To appear in: *LITHOS*

Received date: 5 March 2020

Revised date: 18 June 2020

Accepted date: 20 June 2020

Please cite this article as: A. Vona, C. Romano, G. Giordano, et al., Linking magma texture, rheology and eruptive style during the 472 AD Pollena Subplinian eruption (Somma-Vesuvius), *LITHOS* (2020), https://doi.org/10.1016/j.lithos.2020.105658

Linking magma texture, rheology and eruptive style during the 472 CE Pollena Subplinian eruption (Somma-Vesuvius)

Alessandro Vona[1*], Claudia Romano[1], Guido Giordano [1], Roberto Sulpizio [2,3,4]

[1]Dipartimento di Scienze, Università degli Studi Roma Tre, L.go San Leonardo Murialdo 1, 00146 Roma, Italy

[2] Dipartimento di Scienze della Terra e Geoambientali, Università di Bari, Via Orabona, 4, 70125 Bari, Italy

[3] IGAG-CNR, via Mario Bianco 9, 20131 Milano, Italy

[4] Istituto Nazionale di Geofisica e Vulcanologia, Via Donato Creti 12, 40128 Bologna, Italy

*Corresponding author (alessandro.vona@uniroma3.it)

Highlights:

- A subplinian eruption is a reference scenario in case of Vesuvius reactivation
- Pyroclast textures are used to reconstruct Pollena subplinian eruption dynamics
- Conduit processes control eruption intensity and fall/PDC transition
- Subplinian and Plinian events at Vesuvius show similar eruptive mechanisms

Keywords: Vesuvius, Subplinian eruptions, Vesicle and Crystal Textures, Magma Viscosity

Lithos

Submitted March 4, 2020

Revised June 18, 2020

Abstract

The study of medium-large magnitude and intermediate-high intensity (VEI = 4/5; Column Height 15-20 km) eruptions fed by poorly evolved magmas is one of the main topics in volcanology. In this framework, the 472 CE (Pollena) eruption from Somma-

Vesuvius (Italy) represents a key case study, as it is one of the subplinian eruptions used to constrain the reference scenario adopted by the Italian Department of Civil Protection in case of renewal activity at Somma-Vesuvius. The Pollena eruption experienced a complex dynamics, with abrupt shifts in eruptive style. This study focused on the fall products (L1-L8) of the magmatic eruptive phases (Phases I and II), which preceded the onset of the final phreatomagmatic phase (Phase III). Phase I was characterized by unsteady magma discharge resulting in an oscillating convective column, whereas Phase II involved pulsating activity with alternation of sustained and collapsing columns. To evaluate the role of textural variability in controlling magma rheology (and therefore variations in magma discharge), a detailed textural analysis of the juvenile products has been performed.

Pyroclast textures record a variable degree of outgassing efficiency and lateral textural stratification of magma in the conduit, related to differential magma ascent rates and resulting in variable eruption intensity. Repetitive patterns of magma densification, achieved by progressive outgassing and crystallization, led to stages of decreasing ascent velocity resulting in the end of the eruptive pulse (during the oscillatory Phase I) or anticipating PDC emplacement (at the end of Phase I and during the pulsatory Phase II). Further decompression of the outgassed magma induced intense clinopyroxene microlite crystallization, that markedly increased magma viscosity and promoted the restoration of sustained columns during the eruption climaxes (L3 and L8). Magma densification patterns and consequent unsteadiness in magma discharge at the surface may derive from small heterogeneities in the initial volatile budget and/or represent a natural evolution of low viscosity magmas, as those feeding Pollena eruption, where efficient crystallization in the conduit can deeply and abruptly modify magma rheology, outgassing ability, conduit flow and, ultimately, eruptive style.

1. Introduction

Subplinian eruptions are characterized by unsteady magma discharge (e.g. Cioni et al., 2015 and references therein), responsible for the formation of short-lived, oscillating convective columns, repeated transitions from sustained to collapsing column (e.g. Trolese et al., 2019), and occasionally time-breaks of days/weeks between different eruptive pulses (e.g. Miyaji et al., 2011). As a result, the pyroclastic fall deposits show alternating grain size, and are frequently interlayered with small-volume pyroclastic density currents (PDC) (e.g., Sulpizio et al., 2005; 2007; Pensa et al., 2015). The unsteady behavior and the associated transitions in eruptive style are commonly ascribed to the decoupling between magma supply at depth and magma discharge at the surface (e.g. Scandone and Malone, 1985) and can be caused by either external or internal factors. External factors involve: i) magma-water interaction (Cioni et al., 2003), and/or ii) syn-eruptive changes of conduit shape (Wilson et al., 1980; Massaro et al., 2018). Internal factors include: iii) changes in physico-chemical parameters of the magma stored in the reservoir (Jaupart and Allegre, 1991; Pensa et al., 2015; Di Piazza et al., 2019; Romano et al., 2020), and/or iv) syn-eruptive change of flow behavior, magma ascent and degassing dynamics along the conduit (Gardner et al., 1998; Wilye et al., 1999, Cioni et al., 2003, Pardo et al., 2014; Romano et al., 2020). All internal factors affect magma rheology, which strongly depends on melt chemical composition (including dissolved volatile content; e.g., Romano et al., 2003; Giordano et al., 2008), crystal and bubble contents (e.g., Mader et al., 2013 and reference therein; Vona et al., 2013, 2016). Multiphase magma rheology, in turn, deeply controls every process during ascent as volatile exsolution, bubble growth, gas escape and degassing

induced crystallization (e.g., Cashman and Blundy, 2000; Gonnermann and Manga, 2007). As a consequence, set the external processes aside, the time-dependent rheological behavior of magmas ultimately determines the style, duration and size of the eruptions, as well as the fluctuations in eruptive intensity often responsible for abrupt transitions in eruptive style (e.g., Campagnola et al., 2016).

We focused our study on the Pollena subplinian eruption of Somma-Vesuvius (Fig. 1; Rosi and Santacroce, 1983; Sulpizio et al., 2005) dated at 472 CE (Rosi and Santacroce, 1983; Andronico et al., 1995). This type of eruption (VEI = 4; Column Height 12-20 km) has a conditioned probability of ~ 30% to take place in case of a renewal of the activity at Vesuvius (Marzocchi et al., 2004), and has been adopted by the Italian Department of Civil Protection as the reference eruptive scenario associated with the emergency plan (DPC, 2012).

Pollena eruption started with a sustained, oscillating column related to magmatic fragmentation (i.e. no external water involved; Phase I in Sulpizio et al., 2005). This Phase ended with the destabilization of the convective column, its collapse and the generation of PDCs. Subsequently, the eruption entered a more complex phase (Phase II in Sulpizio et al., 2005) characterized by the emplacement of several PDCs punctuated by two episodes of powerful convective column. The eruption ended with the emplacement of two PDC deposits generated by phreatomagmatic activity (Phase III in Sulpizio et al., 2005).

In order to evaluate the role of the textural variability in controlling magma rheology and therefore eruptive dynamics (e.g., Cashman and Mangan, 1994), a detailed analysis of the erupted juvenile products has been performed with the aim to define their density, porosity, crystallinity, and their vesicle and crystal size distributions (i.e., VSD and CSD,

respectively). In particular, the purpose of this study was to address the magma textural (and therefore rheological) control on: 1) the oscillating behavior of the convective column during the initial phase of the eruption; 2) the transition from sustained to collapsing column between Phase I and Phase II; 3) the restoration of the high energy sustained column events (and their subsequent collapse) during Phase II.

Moreover, the reconstructed eruption dynamics of the subplinian Pollena eruption was compared to that of the 79 CE Plinian eruption at Vesuvius as inferred by previous studies on pyroclast textures (Gurioli et al., 2005; Shea et al., 2009; 2010a; 2011; 2012; 2014; Balcone-Boissard et al., 2011) to evaluate possible analogies and differences between the products and the eruptive processes of these two main events which characterized the Vesuvius eruptive history.

2. 472 CE Pollena eruption of Somma-Vesuvius

The stratigraphy and petrology of the 472 CE Pollena eruptive products of Vesuvius have been described by Rosi and Santacroce (1983), Arnò et al. (1987); Joron et al. (1987), Mastrolorenzo et al. (2002), Rolandi et al. (2004), and Sulpizio et al. (2005) (Fig. 1).

Bulk rock compositions indicate that the first erupted magma (L1) is phonolitic (Fig. 1D; Sulpizio et al., 2005; Santacroce et al., 2008). During the eruption, magma becomes progressively less evolved (from phonolite to phonotephrite). At Vesuvius, similar chemical gradients are common and have been interpreted as due to a stratified magma

chamber in which the phonolitic magma occupies the apical part of the reservoir (Sigurdsson et al., 1990; Cioni et al., 1995, 1998; Scaillet et al., 2008).

The most recent and detailed stratigraphical study of 472 CE eruption by Sulpizio et al. (2005) has been used as benchmark for this study. The composite stratigraphic section of the erupted products, as reconstructed by the authors is shown in Figure 1B. As for other Plinian and subplinian events of the Somma-Vesuvius, the 472 CE Pollena eruption is characterized by a thick, basal sequence of fall beds covered by PDC deposits in the upper part of the stratigraphic succession (Rosi and Santacroce, 1983). Sulpizio et al. (2005) distinguished three main phases based on the dominant eruptive style (i.e., sustained column vs. pyroclastic density currents, PDC) and the type of fragmentation (i.e., magmatic vs. phreatomagmatic) driving the eruptive dynamics.

The first phase of the eruption (Phase I) is characterized by a continuous succession of fall beds of variable grain-size (lapilli-dominated: L1 to L7; and ash-dominated: A1-A4). Except for the L1-L2 and L6-L7 transitions, all lapilli beds are separated by thin ash layers (A1-A4; Fig. 1B) indicative of short period of times in which the eruptive column is absent or significantly lowered. Phase II is characterized by the alternation of PDC and fall deposits, the latter indicated as L8 and L9 (Fig. 1B). Both Phases I and II do not show any evidence of phreatomagmatic fragmentation (Rosi and Santacroce, 1983; Sulpizio et al., 2005). Conversely, as commonly observed in other explosive eruptions from Vesuvius (Santacroce et al., 2008 and references therein), extensive phreatomagmatic activity characterizes the final phase of the eruption (Phase III), which is dominated by dilute and dense PDC deposition (Rosi and Santacroce, 1983).

In this study, we focused our attention on the fall products from Phase I and II. In general, all these deposits vary in thickness and lithology throughout the stratigraphic sequence and show a northeastward dispersal with variably elongated isopachs (Fig. 1A; Sulpizio et al., 2005). The variability of dispersal and grain size oscillations reflects the effect of the unsteady subplinian column.

The first member of the Pollena eruption (L1) is a massive, well-sorted, lapilli sized fall deposit, characterized by highly vesicular juvenile fragments (mainly light-colored pumices of phonolitic composition; Fig. 1D) and scarce accidental lithic clasts. Column height (h) and mass discharge rate (MDR), estimated by Sulpizio et al. (2005) by means of the Carey and Sparks (1986) method, correspond to h = 13 km and MDR = $9x10^6$ kg s^{-1}. All the following fall beds (L2-L9) are dominated by angular, crystal-bearing dark-grey scoria lapilli showing less evolved compositions (Fig. 1D). L2 and L3 are separated by A1 bed in proximal sites, and merge in medial and distal sites to form a single layer. In L2 and L3 beds, the abundance of accidental lithic fragments (mainly lava fragments) sharply increases, suggesting crater enlargement (Sulpizio et al., 2005). Calculated column height and MDR for L2-L3 layer increase to h = 16 km and MDR = $2x10^7$ kg s^{-1}, respectively. The amount of accidental lithics decreases in the overlaying L4 bed, which shows grain-size oscillations upwards. For this bed, calculated column height and MDR show the lowest values (h = 12 km and MDR = $7x10^6$ kg s^{-1}). L5 and L6 beds are massive, well-sorted lapilli units, comprising dark gray scoriae. As L4 bed, they are also characterized by low accidental lithic/juvenile ratios, although increase in lithic size results in higher calculated column height (L6 bed; h = 14 km and MDR=1.2 $x10^7$ kg s^{-1}). The fall deposit closing Phase I (L7) also consists in a massive, well-sorted lapilli unit, although the abundance of

accidental lithics (mainly hydrothermally altered lava fragments) increases. Its limited dispersal area (Fig. 1A) testifies a lowering of the convective column during the emplacement of this bed (Sulpizio et al., 2005).

Two main fall beds (L8 and L9) characterize the second phase of activity (Phase II), that consists in an alternation of PDC and fall deposits. The L8 fall bed records the highest magnitude and intensity of the whole eruption (h = 20 km and MDR=3.4 $x10^7$ kg s^{-1}) and consists of well-sorted lapilli, including dark colored scoriae and deep-seated accidental lithic fragments of syenites, marbles, cumulates and skarns, indicative of a deepening of the fragmentation process (Barberi et al., 1989). Phase II is closed by the deposition of L9 fall bed, made of well-sorted lapilli characterized by a low amount of accidental lithics (mainly lava fragments), and resulting from a powerful subplinian convective column similar to L8 (Sulpizio et al., 2005).

3. Sampling and methods

The samples used for the textural analyses were collected at the "Vergine di Castello" site (Fig. 1A), corresponding to VS7 section of Sulpizio et al. (2005). This section is located on the NE flank of Mt. Somma (i.e. along the maximum dispersal axis) at ~ 4 km from the eruptive vent and shows the best exposure of the fall deposits of Phase I (L1-L7) and of L8 bed of Phase II (Fig. 1C). Due to post depositional erosion affecting L9 bed in both proximal and medial/distal sites, we decided to exclude this layer from our analysis.

Between 1 and 2 kg of pyroclastic material was collected for each stratigraphic layer (Fig. 1C). For two thick fall beds (L4 and L8), samples at different stratigraphic height have been collected (L4B, L4M and L4T for L4 bed, and L8B and L8T for L8 bed; where B, M and T suffixes label the bottom, middle and top stratigraphic positions, respectively). Samples were mechanically dry-sieved at 1 Φ intervals ($\Phi = -\log_2 D$, where D is the particle diameter in millimeters). Grain size distribution data (Fig. 1F) were used to identify the grain size $-3 < \Phi < -2$ as the most representative and suitable for density/vesicularity determination and quantitative textural analyses (see Sulpizio et al., 2005, for a more detailed grain size characterization of the eruption).

For each level, density measurements were performed on 100 vesicular juvenile clasts following the method of Houghton and Wilson (1989). Clast densities were converted into vesicularities using dense rock equivalent (DRE) densities of 2.57-2.75 g cm^{-3}, as measured by helium pycnometry on sample powders. Connected and bulk (i.e. connected + isolated) porosities were obtained by comparing water and dry weights of clasts before and after a coating with a waterproofing spray (density of solidified spray of 1.20 g cm^{-3}). Ratio between connected and bulk porosity corresponds to the pore connectivity as defined in Colombier et al. (2017). Pore connectivity of all the analyzed clasts (N>1000) spans a wide range of values from about 0.5 (half of the vesicles are isolated) to unity (all the vesicles are connected). Values higher than unity have no physical meaning (see Colombier et al., 2017) and give a measure of the extent of possible analytical errors in connected vs. isolated porosity and hence *C* estimations.

Following the method of Shea et al. (2010b), density/vesicularity distributions were binned and plotted on histograms, used to select clasts for quantitative textural analysis

(crystal and vesicle size distributions). About 5–10 juvenile clasts from each sample representing the mode (MD), the low- (LD) and the high- (HD) density tails were chosen for each sample. Modal clasts are commonly assumed to be representative of the bulk of the magma erupted at a given time and allow inter-layer comparisons. Conversely, low- and high-density clasts give information on the degree of magma heterogeneity during a specific eruptive event (Sable et al., 2006).

Clasts were mounted in epoxy resin and prepared as polished thin sections for scanning electron microscopy (Philips XL30 SEM at the LIME laboratory of Roma Tre University). Sets of nested BSE images were acquired at four magnifications (20x, 80x, 320x and 640x; image resolution of 114, 460, 1840, 3675 pixels/mm, respectively) and were processed using ImageJ software (imagej.nih.gov/ij/). To characterize vesicle populations in terms of Volume Vesicle Distribution (VVD) and Vesicle Number Density (VND), the Matlab©-based software FOAMS by Shea et al. (2010b) was used. A similar procedure was employed for the characterization of the crystal population in terms of crystallinity, Crystal Volume Distribution (CVD), Crystal Size Distribution (CSD), and Crystal Number Density (CND). Quantitative textural analysis of crystals was only performed on modal density clasts. Crystal fractions were obtained from an integration of measured image crystallinities at different magnifications using in-house Matlab© codes (see Vona et al., 2017 for detailed methodology). The estimation of mean crystal shapes was performed using CSDslice5 software (Morgan and Jerram, 2006) and the stereological conversion to obtain volume distributions from two-dimensional data was performed using the method of Sahagian and Proussevitch (1998). Crystal Size Distributions (CSD) were calculated using CSDcorrections 1.6 software (Higgins, 2000). If not specified, porosity

data are bulk-referred, whereas all other data retrieved for crystals (crystal fraction, CVD and CND) and for vesicles (VVD and CVD) are always referred to the melt phase alone (e.g., Shea et al., 2010b).

4. Results

Figure 2 summarizes the results of the textural analysis of the erupted products as a function of stratigraphic height. Results include density and porosity distributions (Fig. 2A), pore connectivity (Fig. 2B), vesicle number density (Fig. 2C), crystallinity (Fig. 2D) and crystal number density (Fig. 2E). In the following sections, each category is presented in detail.

4.1. Pyroclast density and porosity distributions

The juvenile material of Pollena eruption has a broad density range, from 0.6 to 2 g cm^{-3} (Fig. 2A). A general increase of mean density can be observed with increasing stratigraphic height. In particular, two end-members can be distinguished. The frequency histogram of L1 bed shows a uniform distribution with a main mode in the range 1.0–1.2 g cm^{-3} and 55-60 vol% porosity (highly to moderately vesicular; Houghton and Wilson, 1989; Fig. 2A). In contrast, the top part of the L8 bed (L8T) shows a well-defined distribution with a main mode in the range 1.4 – 1.6 g cm^{-3} and 40-45 vol% porosity (moderately vesicular; Houghton and Wilson, 1989; Fig. 2A). The remaining fall beds show intermediate features, characterized by uni- or bi-modal distributions and

intermediate modal densities (Fig. 2A). In particular, L2 bed shows a quite wide density distribution showing a clear bimodality involving a low-density mode similar to the modal value of L1 and a second high-density mode similar to the modal value of L8T. All L4 beds (from bottom, middle and top positions) resume unimodal distributions, with different modal densities and distributions indicating an internal, vertical stratification, with denser clasts at the bottom (and partly at the top) and lighter clasts in the middle of the layer. L5 layer shows a high-density tail and a rough bimodal density distribution similar to L2 layer, while in L6 a clear unimodal distribution is restored, with a shape and modal densities resembling the distribution of pumice layer L1. In L7 layer the unimodal distribution is maintained, progressively shifting to higher modal density. The series of PDC deposits (LRPF S1, NA in Fig. 1B; Sulpizio et al., 2005) overlaying L7 layer and marking the transition between Phase I (oscillating convective column) and Phase II (pulsatory convective/collapsing column) was not investigated in this study. L8 layer, representing the restoration of the convective column during Phase II and the maximum intensity of the entire eruption, displays an evident density stratification. L8B shows modal density of 1.2–1.4 g cm^{-3} comparable to L7 (before convective column destabilization) but with a narrower distribution. In L8T bed the distribution shifts toward higher densities representing the high-density end-member recorded through the succession. Similarly to L7, L8 episode ends with a new destabilization and collapse of the column generating widespread PDCs (Fig. 1B).

A detailed analysis of the individual contribution of connected and isolated pores to the bulk porosities indicates that the variability of mean clast porosity with stratigraphic height (Fig. 2a) is accompanied by a variability of isolated pore fraction, as illustrated in

detail in Figure 2B and 3. Most of the clasts from L1 bed have isolated porosity between 5-10% (Fig. 3A) resulting in connectivity parameter C always <1 (Fig. 2B). The abundance of clasts with all connected porosity increases in layers L2 and L3 where most of the clasts have 0-10% isolated porosity (Fig. 3B), i.e., $C \leq 1$ (Fig. 2B). In layers L4 and L5 the mean range of isolated porosity (0-20%) sensibly widens (Fig. 3C,D), but clasts with all pores connected are still present ($C \leq 1$; Fig. 2B). Conversely, from L6 upwards all clasts have a minimum of about 5% non-connected pores ($C < 1$; Fig. 2B). In L6 and L7, most of the clasts have isolated porosities ranging from 5-20% (Fig. 3D), while the range expands up to 25% in L8 layer (both at the bottom and the top; Fig. 2B, Fig. 3E).

4.2. Quantitative analysis of vesicles

Textural analysis has been performed for each stratigraphic level on clasts from the mode and the high- and low-density tails of the density distribution (Fig. 2A). Detailed results are reported in Appendix 1 of the Supplementary Materials and summarized in Table 1. Figure 4 shows representative BSE images and textural results for two selected clasts of modal density from end-member layers L1 (opening phase of the eruption) and L8 (last well-developed sustained column).

Clasts appear macroscopically different, as in L1 deposit they are light-green highly vesicular pumices of phonolitic composition, whilst L8 layer is characterized by denser, dark-green/brown scoria of less evolved phonotephritic composition (Sulpizio et al., 2005). From the microscopic point of view, this difference reflects a different septa thickness increasing from L1 to L8 (Fig. 4A,D). Typical vesicle shape is also quite different with more rounded vesicles characterizing the porosity of L1 clasts, compared to the more

convoluted shapes building the porous framework of L8 clasts. Along the stratigraphy, the transition from pumice-dominated to scoria-dominated deposits is quite sharp at the end of L1. Only L2 layer shows mixed populations of pumices and scoria producing its bimodal density distribution (Fig. 2A). From L3 to L8, light-color pumices disappear and, with few exceptions (e.g., L6), scoria with progressively lower average bulk vesicularity become dominant (Fig. 2A).

Vesicle sizes range from few microns to a maximum of ~ 600 μm in L1 and > 1 mm in L8. In both the representative samples of Figure 4, as well as in most of the analyzed clasts along the Pollena stratigraphy (Appendix 1 of the Supplementary Materials), Vesicle Volume Distributions (VVDs: vesicle volume fraction vs. vesicle diameter size) are unimodal, with a mean vesicle size broadly increasing from L1 to L8 clasts and more in general from the lower to the upper layers of the sequence (Fig. 4B,E). Denser clasts often show asymmetrical, negative-skewed shapes (right-modal and truncated at large sizes; Fig. 4E).

Cumulative Vesicle Volume Distribution (CVVD) diagrams (Fig. 5) are almost sigmoidal as anticipated for nearly unimodal distributions. The distributions show some variability both along the sequence and within the same stratigraphic layer for different clast density (Fig. 5). In Fig. 5A, the vesicularities of modal clasts from significative layers L1, L3, L4M and L8B are compared. Clasts from the other layers display intermediate features. On the ordinate axis all the curves reach the effective vesicularity of the specific clast, highlighting the trend of decreasing porosity from L1 to L3 and from L4M to L8B. Furthermore, the different slopes of the curves reflect different median vesicle size showing

minimum values in L1 (~45-50 μm), maximum values in L3 (~105 μm), with intermediate values for L4M and L8B (~70 μm).

In Fig. 5B-H, cumulative distributions of clasts of low, modal and high density of each layer are reported. For L4 and L8, cumulative curves are also separated for sub-layer stratigraphic position, i.e., bottom, (middle) and top. The variability within a single layer is different for L1 (Fig. 5B), L3 (Fig. 5C) and L8 (Fig. 5H) compared to layers L4 (Fig. 5D), L5 (Fig. 5E), L6 (Fig. 5F) and L7 (Fig. 5G). Clasts of variable porosity of layers L1, L3 and L8, show almost overlapping distributions in the small vesicle part of the curve (<100 μm), indicating that the different clast porosity is exclusively ascribed to the variable contribution of large (>100 μm) vesicles. Conversely, clasts from layers L4 to L7 show wider dissimilarities also within the small vesicle population.

Vesicle Number Densities (VNDs) are in the range of $6.8 \times 10^4 - 7.1 \times 10^5$ mm^{-3} (Fig. 2C; Tab. 1). In this case, even if the lowest values are recorded at the top L8 layer, no clear trend with stratigraphy can be detected.

4.3. Quantitative analysis of crystals

The mineralogical assemblage is constituted by dominant leucite (*lc*) and clinopyroxene (*cpx*) and very minor sanidine, biotite and oxides (Fig. 4; Appendix 1). In this study, quantitative analyses of crystal contents and size distributions have been carried out on leucite and clinopyroxene phases, and the contributions of minor phases have been ignored. In Table 1, crystal contents are listed and separated according to crystal sizes as microlites (2D axis length L < 100 μm), microphenocrysts (100 μm < L < 300 μm) and phenocrysts (L > 300 μm). *Cpx* phenocrysts are common, whilst *lc* phenocrysts are absent

or not statistically relevant and for this reason have not been included in Table 1. Leucite microlites represent the most common and abundant crystalline phase. Leucite crystals are rounded (mean aspect ratio *R* close to unity), while clinopyroxene crystals range from weakly elongated prismatic phenocrysts and microphenocrysts (*R*=2-3) to more elongated microlites (*R*=4-6) (Morgan and Jerram, 2006). An almost continuous increase in crystal content (both *lc* and *cpx*) is observed with increasing stratigraphic height (Fig. 2D) from about 20-25% by volume on vesicle-free basis at the beginning of the eruption (L1) (Fig. 4C) to 45-55% for L8 layer (Fig. 4F). Layer L3 seems to depart from this trend displaying high crystal fractions (40-45%), despite its relatively low stratigraphic position.

Figure 6 displays Cumulative Crystal Volume Distribution (CCVD) diagrams of leucite, clinopyroxene and total crystal content for all the analyzed stratigraphic layers. In all cases, the volume distributions of *lc* phase have a sigmoidal shape, confirming that population is completely described and most of the crystals have sizes lower than ~100 μm. On the contrary, *cpx* populations show linearly increasing distributions in the investigated size range (< 1 mm), testifying the presence of larger phenocrysts not observed due to the size limitation of the analyzed clasts. CVVDs of the whole crystal population (*lc* + *cpx*) maintain however a sigmoidal shape indicating the predominant contribution of leucite crystals to the overall distribution.

Leucite median size (50^{th} percentile of the cumulative distribution; Tab.1) is the largest for L1 layer (50 μm), decreases to a minimum value of 15 μm for L4-L5 layers and slightly increases upwards (25 μm for L8 layer). For clinopyroxene, a rough increase in mean size could be observed from L1 (15-20 μm) to L8 (20-550 μm) although the estimate is biased by the incomplete characterization of the phenocryst population (Tab. 1).

Crystal Size Distribution (CSD) diagrams are reported in Appendix 1. In the classic semi-logarithmic representation, leucite CSDs show almost linear distributions, with a common downward curvature at small sizes. Conversely, clinopyroxene CSDs are curved and concave-up. The slope and intercept of the CSDs have been determined by linear regression and are listed in Tab. 1. A single regression was sufficient to characterize the entire leucite population. In contrast, the curved CSDs of clinopyroxene have been modeled using two linear segments, for microphenocryst (> 100 μm) and microlite populations, respectively (Appendix 1 and Tab.1). For the latter, only the smallest sizes (< 30 μm), not affected by the CSD curvature, were selected for the regression. In L1 and L2 clasts, *cpx* microlites were absent or statistically not significative and only parameters from the large population (> 100μm) were retrieved. Leucite intercepts and slopes vary from 13 to 19 ln mm^{-4} and from -67 to -220 mm^{-1}, respectively. Intercept and slope of *cpx* microphenocrysts range from 10 to 15 ln mm^{-4} and from -18 to -71 mm^{-1}, respectively, whilst intercept and slopes of *cpx* microlites are higher and steeper, ranging from 20 to 22 ln mm^{-4} and from -200 to -280 mm^{-1}, respectively. No clear trend of CSD parameters can be detected along the sequence (Fig. 7A; Tab. 1). On the other hand, Crystal Number Densities (CND) of leucite and clinopyroxene and their variability along stratigraphy show substantial differences (Fig. 2E and Tab. 1). In general, number densities of leucite crystals (~10^3 – 10^4 mm^{-3}) are 1-2 orders of magnitude lower than those of clinopyroxene (~10^4 – 10^6 mm^{-3}). The lowest values of *lc* and *cpx* number densities are both found in L1 layer (CND_{lc}: 4.4 – 6.3 x 10^3 mm^{-3}; CND_{cpx}: 1.2 – 1.9 x 10^4 mm^{-3}). CNDs from L2 layers (CND_{lc}: 2.2 – 2.5 x 10^4 mm^{-3}; CND_{cpx}: 1.4 – 4.6 x 10^4 mm^{-3}) appear similar to L1 or transitional to the values from all the

other stratigraphic layers L3-L8 (CND_{lc}: 2.6 x 10^4 – 3.4 x 10^5 mm^{-3}; CND_{cpx}: 1.0 – 4.3 x 10^6 mm^{-3}).

The comparison of CND and crystal content (Fig. 7B) also highlights a difference between leucite and clinopyroxene populations and their evolution during the eruption. For leucite, a direct relation is evident from L1 to L2 (oblique trend in Fig. 7B), whereas the variation of crystallinity in the L3-L8 interval is accompanied by a narrow range of CND (quite vertical trend in Fig. 7B). On the other hand, a positive correlation can be appreciated for all clinopyroxene data, although an apparent change of slope and a large gap (in the interval $10^5 < CND_{cpx} < 10^6$ mm^{-3}) between L1-L2 and L3-L8 data clusters can be envisaged.

5. Discussion

Similarly to the other major eruptions of Somma-Vesuvius, as the subplinian Greenish Pumice (19 ka; Cioni et al., 2003; Santacroce et al., 2008) and the Plinian 79 CE (Shea et al., 2012), Pollena eruption was characterized by a complex sequence of events with abrupt shifts in eruptive style.

Based on componentry, grain size, microscopic features of the juvenile fragments and field evidences, Sulpizio et al. (2005) ruled out for Phases I and II significative magma-water interaction and major changes in the conduit geometry (failure of conduit walls and successive clearing). With the exclusion of these external environmental processes (e.g., Barberi et al., 1989; Houghton et al., 2004), unsteady magma discharge rates can only be

determined by intrinsic factors able to induce temporal variation of magma flow behavior (Gardner et a., 1998; Cioni et al., 2003). These factors include variations in physico-chemical parameters of magma stored in the reservoir providing the overpressure driving the eruption (e.g., temperature, chemical composition, volatile budget) and/or transformations (e.g., vesiculation and crystallization) occurring during magma ascent toward the surface.

The 472 CE Pollena deposits exhibit an almost continuous bulk compositional variation from phonolite to leucititic phonotephrite (Rosi and Santacroce, 1983; Cioni et al., 1998; Fig. 1D). At Vesuvius, a composition and temperature gradient (ranging from T~850-900 °C for the more evolved melt to T~1050 °C for the more mafic melt; Cioni et al., 1998), is expected for relatively large magma chambers, as those inferred for Pollena (0.1-0.5 km^3, Cioni et al., 1998).

Initial volatile content of magma feeding Pollena eruption is less constrained. Relatively high water contents were recorded in MI (> 5-6 wt.%; Fulignati and Marianelli, 2007) with no significant changes between the phonolitic (L1) and the phonotephritic (L8) end members. At the same time, slight variations in the initial dissolved volatile content along the entire sequence (e.g., L2-L7) could exist and could have played a role in modulating magma supply (e.g., Jaupart and Allegre, 1991). In fact, initial volatile content exerts a primary control on the ascent dynamics, affecting melt viscosity and the entire degassing process (e.g., bubble nucleation and growth, degassing induced crystallization, gas permeability onset), in turn determining the magma ascent velocity (including the onset of lateral velocity gradients), the effective MDR, as well as the waning and ending of a single eruptive pulse.

The effects of all the conduit processes are frozen in the textures of the erupted pyroclasts. In the following, we analyze and discuss all the textural information to get insights on the influence of conduit processes on the eruptive dynamics, and in particular on the oscillating behavior of the eruptive column (including phases of ash production) during Phase I, as well as the column collapse at the end of Phase I and during the pulsating activity of Phase II.

5.1. Conduit processes inferred by pyroclast textures

A large textural variability in terms of clast morphology, porosity, crystallinity, vesicle and crystal size distributions has been observed in the juvenile fragments of the 472 CE Pollena eruption both along the stratigraphy and within each single layer (Fig. 2-7 and Appendix 1). In the following sections, information from vesicle and crystal populations are first discussed separately and then merged to get a complete picture of the textural variations and their link to the complex dynamics generating the Pollena eruption.

5.1.1 Inferences from vesicle populations

In all the analyzed dataset, Vesicle Volume Distributions (VVDs) are mostly unimodal (Figs. 4-5, and Appendix 1) suggesting a relatively simple history of bubble nucleation and growth (Klug et al., 2002), whereas Vesicle Number Densities (VNDs) are in the range of 10^4-10^6 mm^{-3} (Fig. 2C; Tab. 1), which represents typical values for subplinian eruptions fed by evolved magmas (e.g., Di Piazza et al., 2019) or Plinian eruptions from more mafic compositions (e.g., Sable et al., 2006, and references therein).

Along the analyzed sequence, the most important textural variations related to the bubble population involve changes in mean pore connectivity (Fig. 2B and 3) and vesicle median sizes (Fig. 5), both concurring to determine the different bulk clast porosities (Fig. 2A).

The pore connectivity parameter, representing the connected fraction of total porosity (Fig. 2B, 3), can be used as a simplified proxy for magma permeability (Formenti and Druitt, 2003; Giachetti et al., 2010; Bouvet de Maisonneuve et al., 2009; Shea et al., 2012; Colombier et al., 2017). This simplification is related to the independence of connectivity from pore aperture size and tortuosity, fundamental parameters controlling the evolution of gas permeability (e.g. Saar and Manga, 1999; Blower, 2001; Polacci et al., 2006).

Isolated porosity substantially changes within each eruptive unit, both in the minimum value (from 0 to 10%) and in the range of values of the investigated clast populations (up to 50%). In analogy with previous studies (e.g., Shea et al., 2012; 2014), we interpret the measured variability as related to different degrees of maturation of the bubble network by free growth, coalescence of medium to large bubbles, development of permeable outgassing and subsequent collapse prior to magma fragmentation. Extensive coalescence is responsible for the increasing connectivity in some of the analyzed clasts (from L1 to L2-L3; Fig. 3); once volatiles are lost through outgassing, bubbles collapse and magma heals leaving several isolated bubbles, as indicated by the general lower *C* value (L6-L8; Fig. 2B and 3D,E) and VVD truncated shape (L8; Fig. 4E). A maturation of bubble population during the eruption is confirmed by the increase of vesicle median sizes (e.g., from L1 to L2-3 and from L7 to L8), possibly related to the higher amount of time allowed for bubble growth (e.g., Adams et al., 2006).

Intra-layer porosity distribution in L1 and L8 layers seems to be dictated by a change in the large size population (see CVVDs in Fig. 5B,H), while the small size population substantially overlaps. This population distribution is in agreement with the different density clasts sampling magma with variable degree of bubble coalescence, but relatively uniform ascent velocities (e.g., Gurioli et al., 2005). Conversely, more complex patterns characterize the Vesicle Volume Distributions of L2 and L4-L7 layers with differences in both small and large size populations (Fig. 5B-G). In this case, a possible interpretation involves more marked differential ascent velocities across the conduit and therefore variable residence time of different magma parcels able to produce large radial gradient of vesicularity and VSD (Polacci et al., 2001; Houghton et al., 2004; Adams et al., 2006; Sable et al., 2006; Noguchi et al., 2006; Shea et al., 2012). This type of intra-layer variability is typical of subplinian eruptions (e.g., Pistolesi et al., 2017; Di Piazza et al., 2019), probably related to relatively narrow conduits (i.e., large boundary effects at the margin) leading to large physical gradients in the ascending magma (Cioni et al., 2015).

In addition to lateral vesicularity gradients, the multiple sampling at different stratigraphic heights within the same layer (i.e., L4 and L8) shows a vertical vesicularity stratification (Fig. 2A), likely recording conduit processes acting during the single eruptive pulse (e.g., Di Piazza et al., 2019). In both L4 and L8 cases, a shift to higher modal pyroclast density (modal densities of 1.27 and 1.47 g cm^{-3}, respectively) marks the end of the eruptive pulse. For L4, the intermediate layer L4M shows the lowest pyroclast density (1.05 g cm^{-3}). A sequence of processes able to produce such variations could be: 1) relatively high degree of open-system degassing at the beginning of the eruptive pulse, generating heterogenous density distributions (e.g., L4B, and in part L8B); 2) more coupled

degassing in the central part of the eruptive pulse representing the maximum intensity (L4M and L8B) (e.g., Sable et al., 2006); 3) magma ascent velocity decreasing, higher degree of gas-magma decoupling and gas escaping at the end of the eruptive pulse (L4T and L8T) (e.g., Adams et al., 2006).

Trends of progressive magma densification similar to those within L4 and L8 layers can also be observed from L1 to L2, and from L6 to L7 layers (Fig. 2A), which are not separated by ash deposition (Fig. 1B) and likely recorded a general decrease of magma ascent rate across the transitions.

Therefore summarizing, several cycles of magma densification can be envisaged throughout the stratigraphical record both within a single pulse (L4 and L8) and within contiguous lapilli beds (L1-L2, L6-L7). During the first part of the eruption (L1-L2 and-L4B-L4T), the eruptive pulses end with the deposition of ash layers (A1 and A3, following L2 and L4, respectively; Fig. 1B) indicative of a repose time at the end of these pulses. Subsequently, activity resumed with the eruption of high-density magma (L3 and L5, respectively), possibly recording a previous stage of magma stalling, and in turn ended with a new ash deposition phase (A2 and A4, respectively). Conversely, in the final part of Phase I (L6-L7), magma densification anticipates the destabilization of the sustained column and the generation of PDCs. A new episode of magma stalling, likely following the PDC formation, was interrupted by a magma remobilization corresponding to L8 phase of the eruption. As at the end of L7, L8 magma densification leads to the subsequent column collapse.

5.1.2 Inferences from crystal populations

The overall crystal content increases during the eruption (Fig. 2E). However, the histories recorded by leucite and clinopyroxene are different and provide information on distinct stages of the eruptive process.

Figure 7B can give insights on the crystallization process and its kinetics (Blundy and Cashman, 2008). Generally, a direct relation between crystal content and CND indicates that the crystallization is dominated by crystal nucleation, whose degree is mainly controlled by the decompression rate (e.g., Hammer and Rutherford, 2002). On the contrary, crystal contents increasing without a significant change of CND (vertical trend in Fig. 7B) indicate that crystallization is dominated by growth and crystal content can be used as a proxy for the time spent by the magma at quite steady conditions (e.g., Cashman and Marsh, 1988).

L1 layer is characterized by large leucite micro-phenocrysts (Fig. 6) and the lowest CND (CND_{lc}: 4.4 – 6.3 x 10^3 mm^{-3}; Fig. 7B), both indicating relatively low degrees of undercooling for the phonolitic magma. L2 layer displays intermediate values of both crystal size and CND, whereas from L3 to L8 layers leucite crystals are smaller and have a higher CNDs (CND_{lc} 3.0 x 10^4 – 3.4 x 10^5 mm^{-3}), quite constant and independent of stratigraphic layer. This latter trend can be interpreted as a growth-dominated crystallization under almost constant undercooling conditions (greater than in L1). Within the L3- L8 layers, the difference in leucite content is therefore mostly related to variable crystallization time.

Through decompression experiments on 79 CE eruption material, Shea et al. (2009) ruled out leucite formation during fast magma ascent in the conduit and proposed that leucite microphenocrysts more likely crystallized in magma chamber and/or during an

initial stage of slow decompression preceding the eruption. We used the range of leucite growth rates experimentally derived by Shea et al. (2009) ($G_{lc(min)}$ = 2x10^{-8} mm s^{-1}; $G_{lc(max)}$ = 1x10^{-7} mm s^{-1}) and the CSD slopes (Tab. 1) to constrain the crystallization timescales ($\tau = -1/G \times slope_{CSD}$; Marsh, 1988; Cashman and Marsh, 1988) of leucite during Pollena eruption (Fig. 8). Timescales span from 13 hours to 9 days. No clear trend can be recognized with stratigraphy, due to the relatively small CSD slope variation (Tab. 1). The results of the calculation suggest however that also in the case of Pollena eruption, leucite crystallization occurs before the rapid magma ascent in the conduit.

Conversely, beside the phenocryst population likely formed in the magma reservoir, clinopyroxene microlites and microphenocrysts analyzed in this study show a general (i.e., not continuous) CND increase during the eruption, ultimately responsible for the increase in crystal fraction, and likely recording the fast decompression stage along the conduit before fragmentation. As for leucite, also clinopyroxene data suggest a different history between the first (L1-L2: low CNDs) and the second part of the eruption (L3-L8: high CNDs).

To calculate the *cpx* crystallization timescales, small (i.e., <30 μm) and large (>100 μm) size populations have been considered separately (Tab. 1; Fig 8). Even in this case, a range of experimentally derived growth rates was selected. In the absence of kinetics data on *cpx* from alkaline compositions similar to Pollena magmas, we selected G values from decompression experiments on basalts and basaltic andesites, and in particular from Shea and Hammer (2013) ($G_{cpx(min)}$ = 2x10^{-6} mm s^{-1}) and from Arzilli et al. (2019a) ($G_{cpx(max)}$ = 2x10^{-4} mm s^{-1}). *Cpx* microphenocrysts (>100 μm) yield crystallization times ranging from few minutes to 8 hours, whereas microlites (< 30 μm), only modeled from L3 to L8 layers,

yield shorter timescales between ~20 seconds and 40 minutes (Fig. 8). These calculations confirm the hypothesis that both *cpx* microphenocrysts and microlites form during ascent along the conduit, with the microlite population likely recording the ultimate decompression before fragmentation.

5.1.3 Combining information from vesicle and crystal textures

Analysis of crystal textures suggest that pyroxene phenocrysts and leucite microphenocrysts were already present during the fast decompression associated with magma ascent in the conduit, when conversely, extensive crystallization of clinopyroxene microlites and microphenocrysts took place. VVDs suggest a relatively simple vesiculation history, in which volatile exsolution is mostly limited to the final ascent and involves variable degrees of maturation of bubble population by free growth, coalescence, permeability onset, outgassing and bubble collapse (Fig. 4,5).

Figure 9 compares crystallinity and bulk porosity for the analyzed clasts. As argued by Gurioli et al. (2005), a positive correlation might indicate heterogeneous bubble nucleation on microphenocrysts (e.g., Hurwitz and Navon, 1994), whereas an inverse relationship would point to a role of crystals in hampering bubble growth and expansion (e.g., Gardner et al. 1998). No simple relationship can be inferred between crystallinity and bulk porosity (Fig. 9A). Vesicle fraction referred to the melt phase alone (i.e., calculated on a crystal free basis; Fig. 9B) gives a measure of the effective gas fraction available for magma fragmentation. In this case, with the exception of the outlier L5 layer, a better-defined positive correlation characterizes data distribution throughout the eruption from L1 (low values of crystallinity and melt-referenced porosity) to L8 (higher values of both). It is

interesting to note that layers with high melt-referenced porosity and crystallinity are also those with lower vesicle connectivity (Fig. 2B).

Highly explosive activity (coupled degassing and overpressurized bubbles) is favored by fast magma rise, high decompression rates, high viscosity of the magma or a coupling of these factors (Houghton et al. 2004). Syn-eruptive crystallization of abundant microlite probably played a key role in enhancing coupled degassing by increasing the effective viscosity of the magma during its ascent. A similar model is commonly accepted as the most reliable for highly explosive mafic eruption (Sable et al., 2006; Szramek, 2016; Arzilli et al., 2019a,b; Bamber et al., 2020). In particular, the crystallization timescales of *cpx* microlites (Fig. 8) in the order of seconds to minute are consistent with timescales inferred for syn-eruptive disequilibrium crystallization in explosive eruptions fed by poorly evolved (basaltic) magmas (La Spina et al., 2016; Arzilli et al., 2019a).

To verify how much suitable a similar mechanism could be for Pollena eruption, calculations on the effective viscosity (η_{L+C}) of the involved magmas have been performed. Melt viscosity (η_L) was calculated on chemical basis (Sulpizio et al., 2005) using the GRD model by Giordano et al. (2008) and a constant value of 1.5 wt.% H_2O, as measured in matrix glasses by Mastrolorenzo and Pappalardo (2006). The effect of crystals, expressed as relative viscosity ($\eta_r = \eta_{L+C} / \eta_L$), was derived by the equation of Vona et al. (2011) as a function of crystal content and mean shape (Tab. 1).

Figure 10 shows the results of the modeling for the effect of crystals. Relative viscosities span almost 4 orders of magnitude from η_r ~3 (L1 layer) to 12000 (L8T layer) and show an irregular increasing pattern along the eruption, characterized by minimum values for L1 and L4, relative maximum at L2-L3, and increasing values from L6 to L8.

The striking similar pattern of the computed viscosities and the stratigraphical variation of field-derived MDRs by Sulpizio et al. (2005) (Fig. 10) seems to support a pivotal role of the crystal-bearing magma viscosity to the eruptive dynamics.

More calculations were performed to take also into account possible variations of the bulk viscosity of erupted magmas due to the different melt composition, which vary from phonolite L1 to phonotephrite L8 (Sulpizio et al., 2005), and temperatures, which vary from 850 °C (L1) to 1050 °C (L8) (Cioni et al., 1998).

Figure 11A illustrates the results as a function of temperature. As expected, pure liquid viscosity decreases with stratigraphic height (Fig. 11A, dashed lines) in response to a decreasing of melt polymerization (Romano et al., 2003; Giordano et al., 2008). The relation mostly inverts however, for bulk (i.e., two-phase) viscosity curves when crystals are taken into account (Fig. 11A, solid lines; cf. also Fig. 10). An exception to the trend is represented by L3, whose elevated crystal content results in bulk viscosities higher than all the contiguous layers. To account for the thermal stratification of the Pollena chamber suggested by Cioni et al. (1998), we selected a constant T gradient from T = 850 to 1050 °C, from L1 to L8 magmas (dots in Fig. 11A). The presence of crystals seems to be of greater importance than temperature variation in determining the relative variability of bulk viscosity among the different stratigraphic layers. As a consequence, a direct correlation of effective viscosity with the eruption energy expressed by the MDR still holds, despite the modelled increase in T (Fig. 11B), indicating that the crystal content and its effect on effective viscosity are the main factor controlling explosivity during Pollena eruption, whereas other variables, such as temperature and suspending melt composition, seem to have a smaller effect.

5.2. Magma dynamics during the Pollena eruption

A comprehensive framework of magma dynamics during Pollena eruption can be obtained integrating textural data with field observation (Sulpizio et al., 2005) (Fig. 12).

The eruption started with the emission of L1 phonolite (Fig. 12A), representing the apical part of a chemically stratified magma chamber. Vesiculation process occurred during L1 phase is consistent with a closed-system, near equilibrium degassing up to fragmentation. The narrow density/vesicularity distribution of the pumices suggests a texturally uniform magma (Fig. 4B). This is also confirmed by clasts of different density showing similar small-size vesicle population and only differing in the amount of large coalesced vesicles (Fig. 5B). Leucite crystals show the largest median sizes (35-55 μm) and the lowest CND (4-5 x 10^3 mm^{-3}) of the whole sequence, suggesting that crystallization occurred at relatively low undercooling conditions, in the magma chamber and/or in response to an initial slow decompression (e.g., Shea et al., 2009), 0.5-9 days before the main decompression event (Fig. 3). Clinopyroxene content (< 6%) and CND (CND_{cpx}: 1.2 – 1.9 x 10^4 mm^{-3}) are the lowest of the entire eruption, likely reflecting a subordinate role of *cpx* in this phase of the eruption.

A first change in eruption intensity took place with the emission of L2-L3 layers. An increase in MDR and eruptive column height (from 7x10^6 kg s^{-1} to 2x10^7 kg s^{-1} and from 13 km to 16 km, respectively) is accompanied by the increase in lithic content related to a phase of crater enlargement. Field data do not allow to discern the eruptive energy of L2 and L3 layers, that are separated by an ash layer in proximal sites (Fig. 1B,C), but merge in medial/distal sites (Sulpizio et al., 2005). However, some information can be gathered by

their textural features. The bimodal density distribution of L2 layer (Fig. 2A), characterized by pumices and high density scoria, as well as a clinopyroxene population with CNDs similar to L1 (Fig. 7B), suggest that this layer could represent the final waning stage of the L1 pulse (Fig. 12B). Subsequently, the deposition of the A1 ash layer and the high density of the L3 clasts (Fig. 2A), as well as its relatively high crystal content (Fig. 2D) and mature vesicle textures (large modal size and truncated VVDs; Fig. 5C; Table 1 and Appendix 1) would suggest a brief magma stalling at the end of L2, which allowed the magma to further vesiculate, crystallize and outgas. A subsequent emission of the crystal-rich, degassed high-viscosity magma (Fig. 10-11) would have resulted in the high eruption energy during the L3 phase (Fig. 12C).

The following L4 layer represents the lowest energy phase of the whole eruption (MDR = $7x10^6$ kg s^{-1} and 12 km column height) (Fig. 12B), as consequence of an efficient outgassing and open-system behavior, testified by high connectivity of the analyzed clasts (Fig. 3C) suggesting a low magma supply, possibly related to a slight decrease of the initial volatile content. Low ascent velocities are also correlated to relatively low values of CND (Fig. 7B), melt-referenced gas volume fraction (Fig. 9) and viscosity (Fig. 11) for L4 magma. The textural variability can be successfully explained by marked lateral magma stratification in response to differential ascent velocity (Fig. 5C). After an eruption rest marked by the deposition of the A3 ash layer, L5 clasts display relatively low mean porosity (Fig. 2A) and high VNDs (Table 1) likely recording the previous stage of magma stalling (Fig. 12C).

Layers L6 and L7 show CVVF variability similar to L4 layer indicating the presence of lateral velocity gradients and open system degassing (Fig. 12B). L6 testifies an increase

of eruption energy compared to L4 (h = 14 km and MDR=1.2 x10^7 kg s^{-1}), where the degree of outgassing is reduced as recorded by decreasing vesicle connectivity (Fig. 2B; Fig. 3C,D), increasing crystal fraction (Fig. 2D) and melt-referenced porosity (Fig. 9). With L7, a new densification of the erupted magma (Fig. 2A) is indicative of the incorporation of high abundance of slow-moving magma from the conduit margin (Fig. 12B). In this case, however, magma densification, implying both larger outgassing and an increase of the bulk density of the erupted pyroclastic mixture, leads to the column collapse occurred at the end of the Phase I (LRPF; Sulpizio et al., 2005) soon after the emplacement of L7 layer. A similar mechanism has been invoked for the PDC generation at Vesuvius during the 79 CE eruption (Shea et al., 2012).

During the Phase II, after the emplacement of two additional PDCs (S1 and NA; Sulpizio et al., 2005), a convective column is restored in correspondence of L8 layer deposition (h = 20 km and MDR=2.4 x10^7 kg s^{-1}; Fig. 11C). In analogy with L7 layer, L8 clasts show features of extensive outgassing of a slow-moving magma with uniform ascent velocity (low porosity, Fig. 2A; low vesicle number density, Fig. 2C; truncated VVD, Fig. 4E; large modal bubble size, Fig. 5). Similar to L3 and L5 layers (although no MDR data are available for the latter), the contrasting presence of dense clasts and high MDR would point to an initial magma stalling allowing extensive outgassing and a subsequent new decompression event leading to the magma remobilization. In this case, an extensive, rapid (seconds to minutes, Fig. 8) syn-eruptive crystallization of clinopyroxene microlites is testified by the highest *cpx* CNDs and crystal content (Fig. 7B). As previously inferred for L3 (and likely L5), crystal framework increased the effective viscosity hindering free bubble-growth and favoring the onset of bubble overpressure build-up ultimately promoting

and sustaining magma explosivity (Toramaru, 1995; Mueller et al., 2008). The column height is the highest of the whole eruption, reflecting the highest effective viscosity (Figs. 10,11) and melt-referenced gas volume fraction (Fig. 9) reached by the crystal-rich L8 magma. Finally, as at the end of the deposition of L7, magma densification (L8T) could also be the main cause of the subsequent column collapse.

It is possible to notice a repetitive pattern of the eruption. It started with a texturally uniform magma (as evidenced by the narrow density/vesicularity distribution) which is indicative of a closed-system, near equilibrium degassing. With time, velocity gradients developed inside the conduit, producing lateral textural variability and the onset of permeability and outgassing, likely localized near the conduit walls. In each cycle, increasing textural maturation involved the collapse of coalesced bubbles, density increase, overall velocity decrease, up to the stalling of magma, resulting in the end of the eruptive pulse (ash deposition) or leading to PDC emplacement (as at the end of L7 and L8). Magma densification patterns may derive from non-uniform initial volatile content and/or represent a natural evolution of low viscosity magmas, whose fast reaction kinetics (e.g., crystallization and degassing) make them extremely responsive to subtle changes in physico-chemical intensive parameters (T, P) during ascent under disequilibrium conditions (e.g., La Spina et al., 2016). In these conditions, efficient crystallization in the conduit can deeply and abruptly modify magma rheology, outgassing ability, conduit flow and, ultimately, eruptive style.

5.3. Subplinian vs. Plinian eruptions at Vesuvius: comparison with the 79 CE eruption

Pyroclast textures of the subplinian Pollena eruption (VEI 4; 0.5-1.4 km^3 DRE; Sulpizio et al., 2005) used to elaborate the simplified eruptive model presented in Fig. 12 allowed us to make a comparison with data and models from previous studies (Gurioli et al., 2005; Shea et al., 2009; 2010a; 2011; 2012; 2014; Balcone-Boissard et al., 2011) on the Plinian 79 CE eruption at Vesuvius (VEI 5; 2-3 km^3 DRE; Cioni et al., 2008).

Subplinian eruptions commonly display intensities between 10^5 to 10^7 kg s^{-1}, 1 to 2 orders of magnitude lower than Plinian events (Cioni et al. 2008). For Pollena eruptive event, column heights varied between 12 and 20 km, corresponding to mass discharge rates of $7x10^6$ kg s^{-1} and $3.4x10^7$ kg s^{-1}, respectively. The 79 CE eruption column heights varied between 15 and 33 km, corresponding to mass discharge rates of $8x10^7$ kg s^{-1} and $1.5x10^8$ kg s^{-1}, respectively. Despite these differences, the two eruptions show several similarities, and probably share the main mechanisms controlling eruptive dynamics. Conceptual model in Figure 12 was in fact largely influenced by the model of Shea et al. (2012, 2014) for the 79 CE eruption.

Analogies between the Pollena and 79 CE eruptions, and in general between subplinian and Plinian events at Somma-Vesuvius, were first recognized by Rosi and Santacroce (1983). In particular, both sequences are characterized by a thick, basal sequence of fall deposits followed by PDC deposits interbedded in the upper part of the stratigraphic succession, and show a compositional variability, with an initial eruption of a phonolite magma (L1 for Pollena; EU1-EU2 for 79 CE; eruption units after Cioni et al., 1992) followed by a more mafic composition (L4-L8 for Pollena; EU3-EU4 for 79 CE). The 472 CE magma is however less evolved than the magma feeding 79 CE eruption (in Figure 1D, light grey field indicates bulk chemistry of 79 CE eruption; data from

Santacroce et al., 2008). This difference has been attributed to shallower storage conditions and smaller volume of magma involved in the post-79 CE subplinian eruptions (i.e. 472 CE and 1631 CE; Scaillet et al., 2008).

During the 79 CE eruption, the transition between the two erupted magmas was characterized by a higher degree of instability including a partial column collapse (EU2/3; Cioni et al., 1992) responsible for the destruction of the city of Herculaneum (Gurioli et al., 2002). The instability was likely related to the configuration of the magma reservoir feeding Plinian eruptions, characterized by well-developed twofold layering (Cioni et al., 1998), with marked temperature, composition and, therefore, rheological contrasts across the transition between the apical phonolite and the lower phonotephrite. Conversely, at Pollena, possibly due to a more continuous compositional gradient, such transition (L1-L2-L3) is likely associated to short stasis and restoration of activity with an increase in MDR without evidences of PDC generation.

Density and porosity distributions of pyroclasts from both eruptions point to marked lateral velocity gradient during the oscillating/pulsating column phase (L4-L7 for Pollena; EU3 for 79 CE), suggesting a major control of the open vs. closed system degassing on the eruptive dynamics during this phase of the eruption.

Furthermore, both sequences show a gradual increase in the median density (Gurioli et al., 2005), mostly related to increasing crystal content and outgassing efficiency. Magma densification seems to be the main factor controlling column collapse (at the end of L7 and L8 events at Pollena and within the EU3 member for 79 CE; Shea et al., 2012).

Lastly, the peak intensity is achieved in both eruptions during the emission of the low silica end-member (L8 for Pollena; EU3 for 79 CE), before the total column collapse

linked to the onset of phreatomagmatic activity (Barberi et al., 1989; Sulpizio et al., 2005, 2007). Even if both eruptions are characterized by an increase in leucite content, a major role in the increasing energy of sustained column during L8 event of Pollena has been exerted by the rapid syn-eruptive crystallization of clinopyroxene. This significant crystallization process, absent during the 79 CE event was probably favored by the lower melt viscosity and higher component diffusivity of the silica-poorer Pollena magma.

All considered, it appears that, apart from few specific features mainly related to the lower viscosity of Pollena magmas, the governing processes were very similar between the two eruptions, despite the clear differences in their size. These findings imply that subplinian eruptions can be regarded as low-energy cases of a continuum spectrum (from subplinian to Plinian) of highly-explosive volcanism at Vesuvius.

6. Conclusions

The combination of textural data from the erupted products with field-based data of physical volcanology allowed to present a model for the magma dynamics during the subplinian Pollena eruption. All data converge to a pivotal control of conduit processes in determining magma discharge at the surface, controlling the extremely unsteady character of the eruption. In particular outgassing efficiency, possibly related to variable magma ascent rate, seems to regulate the oscillating behavior during the first phase of the eruption, which laid down L1-L7 layers. During the pulsatory second phase of the eruption, after the destabilization of the eruptive column, the effect of intense crystallization of microlites, and

consequent viscosity increase becomes more important and allows the restoration of high energy sustained column (L8). This process is the main difference between subplinian and Plinian eruption at Vesuvius, probably related to the lower viscosity of magmas involved during Pollena eruption, whose dynamics in this phase is more similar to that of high-energy eruption of mafic compositions (e.g., Etna 122 BCE: Sable et al., 2006; Arzilli et al., 2019a; Calbuco 2015: Arzilli et al., 2019b; Masaya Triple Layer, 2.1 ka: Bamber et al.,2020).

Acknowledgements

This study was supported by INGV-DPC V1 (2014-15) project. The Grant of Excellence Departments, MIUR-Italy (ARTICOLO 1, COMMI 314 - 337 LEGGE 232/2016) is also gratefully acknowledged. S. Campagnola, E. Conventi, P. Martizzi, A. Pontesilli, and M. Siciliano are greatly thanked for their support in the laboratory analysis.

References

1. Adams, N.K., Houghton, B.F., Hildreth, W., 2006. Abrupt transitions during sustained explosive eruptions: examples from the 1912 eruption of Novarupta, Alaska. Bull. Volcanol. 69, 189–206. https://doi.org/10.1007/s00445-006-0067-4
2. Andronico, D., Calderoni, G., Cioni, R., Sbrana, A., Sulpizio, R., Santacroce, R., 1995. Geological map of Somma-Vesuvius volcano. Periodico di Mineralogia 64, 77–78
3. Arnò, V., Principe, C., Rosi, M., Santacroce, R., Sbrana, A., Sheridan, M.F. 1987. Eruptive history. In: Santacroce, R. (ed) Somma-Vesuvius. CNR Quad. Ric. Sci. 8 114, 53–103.

4. Arzilli, F., La Spina, G., Burton, M.R., Polacci, M., Le Gall, N., Hartley, M.E., Di Genova, D., Cai, B., Vo, N.T., Bamber, E.C., Nonni, S., Atwood, R., Llewellin, E.W., Brooker, R.A., Mader, H.M., Lee, P.D., 2019a. Magma fragmentation in highly explosive basaltic eruptions induced by rapid crystallization. Nat. Geosci. https://doi.org/10.1038/s41561-019-0468-
5. Arzilli, F., Morgavi, D., Petrelli, M., Polacci, M., Burton, M., Di Genova, D., Spina, L., La Spina, G., Hartley, M.E., Romero, J.E., Fellowes, J., Diaz-Alvarado, J., Perugini, D., 2019b. The unexpected explosive sub-Plinian eruption of Calbuco volcano (22–23 April 2015; southern Chile): Triggering mechanism implications. J. Volcanol. Geotherm. Res. 378, 35–50. https://doi.org/10.1016/j.jvolgeores.2019.04.006
6. Balcone-Boissard, H., Boudon, G., Villemant, B., 2011. Textural and geochemical constraints on eruptive style of the 79 ad eruption at Vesuvius. Bull. Volcanol. 73, 279–294. https://doi.org/10.1007/s00445-010-0409-
7. Bamber, E.C., Arzilli, F., Polacci, M., Hartley, M.E., Fellowes, J., Di Genova, D., Chavarría, D., Saballos, J.A., Burton, M.R., 2020. Pre- and syn-eruptive conditions of a basaltic Plinian eruption at Masaya Volcano, Nicaragua: The Masaya Triple Layer (2.1 ka). J. Volcanol. Geotherm. Res. 392, 106761. https://doi.org/10.1016/j.jvolgeores.2019.106761
8. Barberi, F., Cioni, R., Rosi, M., Santacroce, R., Sbrana, A., Vecci, R., 1989. Magmatic and phreatomagmatic phases in explosive eruptions of Vesuvius as deduced by grain-size and component analysis of the pyroclastic deposits. J. Volcanol. Geotherm. Res. 38, 287–307. https://doi.org/10.1016/0377-0273(89)90044-9
9. Blower, J.D., 2001. Factors controlling permeability-porosity relationships in magma. Bull. Volcanol. 63, 497–504. https://doi.org/10.1007/s004450100172
10. Bouvet de Maisonneuve, C., Bachmann, O., Burgisser, A., 2009. Characterization of juvenile pyroclasts from the Kos Plateau Tuff (Aegean Arc): Insights into the eruptive dynamics of a large rhyolitic eruption. Bull. Volcanol. 71, 643–658. https://doi.org/10.1007/s00445-008-0250-x

11. Blundy, J.D., Cashman, K. V, 2008. Petrologic reconstruction of magmatic system variables and processes. Rev. Mineral. Geochemistry 69, 179–239. https://doi.org/10.2138/rmg.2008.69.6
12. Campagnola, S., Romano, C., Mastin, L.G., Vona, A., 2016. Confort 15 model of conduit dynamics: applications to Pantelleria Green Tuff and Etna 122 BC eruptions. Contrib. to Mineral. Petrol. 171, 60. https://doi.org/10.1007/s00410-016-1265-5
13. Carey, S., Sparks, R.S.J., 1986. Quantitative models of the fallout and dispersal of tephra from volcanic eruption columns. Bull. Volcanol. 48, 109–125. https://doi.org/10.1007/BF01046546
14. Cashman, K. V, Blundy, J.D., 2000. Degassing and crystallization of ascending andesite and dacite. Philos. Trans. R. Soc. London A 358, 1487–1513.
15. Cashman, K. V, Mangan, M.T., 1994. Physical aspects of magmatic degassing II, Constraints on vesiculation processes from textural studies of eruptive products. Rev. Mineral. Geochemistry 30.
16. Cashman, K. V, Marsh, B.D., 1988. Crystal size distribution (CSD) in rocks and the kinetics and dynamics of crystallization II: Makaopuhi lava lake. Contrib. to Mineral. Petrol. 99, 277–291. https://doi.org/10.1007/BF00375362
17. Cioni, R., Marianelli, P., Sbrana, A., 1992. Dynamics of the A.D. 79 eruption: stratigraphic, sedimentological and geochemical data on the successions from the Somma-Vesuvius southern and eastern sectors. Acta Vulcanol. 2, 109–123.
18. Cioni, R., Civetta, L., Marianelli, P., Metrich, N., Santacroce, R., Sbrana, A., 1995. Compositional layering and syn-eruptive mixing of a periodically refilled shallow magma chamber: The AD 79 plinian eruption of vesuvius. J. Petrol. 36, 739–776. https://doi.org/10.1093/petrology/36.3.739
19. Cioni, R., Marianelli, P., Santacroce, R., 1998. Thermal and compositional evolution of the shallow magma chambers of Vesuvius: Evidence from pyroxene phenocrysts and melt inclusions. J. Geophys. Res. 103, 18277–18294.
20. Cioni, R., Sulpizio, R., Garruccio, N., 2003. Variability of the eruption dynamics during a Subplinian event: the Greenish Pumice eruption of Somma–Vesuvius

(Italy). J. Volcanol. Geotherm. Res. 124, 89–114. https://doi.org/10.1016/S0377-0273(03)00070-2

21. Cioni, R., Bertagnini, A., Santacroce, R., Andronico, D., 2008. Explosive activity and eruption scenarios at Somma-Vesuvius (Italy): Towards a new classification scheme. J. Volcanol. Geotherm. Res. 178, 331–346. https://doi.org/10.1016/j.jvolgeores.2008.04.024
22. Cioni, R., Pistolesi, M., Rosi, M. 2015. Plinian and Subplinian Eruptions. In: Sigurdsson, H., Houghton, B., Rymer, H., Stix, J., McNutt, S. (Eds.), The Encyclopedia of Volcanoes, 2nd edn., Academic Press, San Diego, 519–535.
23. Colombier, M., Wadsworth, F.B., Gurioli, L., Scheu, B., Kueppers, U., Di Muro, A., Dingwell, D.B., 2017. The evolution of pore connectivity in volcanic rocks. Earth Planet. Sci. Lett. 462, 99–109. https://doi.org/10.1016/j.epsl.2017.01.011
24. Di Piazza, A., Vona, A., Mollo, S., De Astis, G., Soto, G.J., Romano, C., 2019. Unsteady magma discharge during the "El Retiro" subplinian eruption (Turrialba volcano, Costa Rica): Insights from textural and petrological analyses. J. Volcanol. Geotherm. Res. 371, 101–115. https://doi.org/10.1016/j.jvolgeores.2019.01.004
25. DPC, 2012. Scenari eruttivi e livelli di allerta per il Vesuvio. Italian Department of Civil protection, Rome.
26. Formenti, Y., Druitt, T.H., 2003. Vesicle connectivity in pyroclasts and implications for the fluidisation of fountain-collapse pyroclastic flows, Montserrat (West Indies). Earth Planet. Sci. Lett. 214, 561–574. https://doi.org/10.1016/S0012-821X(03)00386-8
27. Fulignati, P., Marianelli, P., 2007. Tracing volatile exsolution within the 472 AD "Pollena" magma chamber of Vesuvius (Italy) from melt inclusion investigation. J. Volcanol. Geotherm. Res. 161, 289–302. https://doi.org/10.1016/j.jvolgeores.2006.12.011
28. Gardner, C.A., Cashman, K. V, Neal, C.A., 1998. Tephra-fall deposits from the 1992 eruption of Crater Peak, Alaska: implications of clast textures for eruptive processes. Bull. Volcanol. 59, 537–555. https://doi.org/10.1007/s004450050208

29. Giachetti, T., Druitt, T.H., Burgisser, A., Arbaret, L., Galven, C., 2010. Bubble nucleation, growth and coalescence during the 1997 Vulcanian explosions of Soufrière Hills Volcano, Montserrat. J. Volcanol. Geotherm. Res. 193, 215–231. https://doi.org/10.1016/j.jvolgeores.2010.04.001
30. Giordano, D., Russell, J.K., Dingwell, D.B., 2008. Viscosity of magmatic liquids: A model. Earth Planet. Sci. Lett. 271, 123–134. https://doi.org/10.1016/j.epsl.2008.03.038
31. Gonnermann, H.M., Manga, M., 2007. The Fluid Mechanics Inside a Volcano. Annu. Rev. Fluid Mech. 39, 321–356. https://doi.org/10.1146/annurev.fluid.39.050905.110207
32. Gurioli, L., Cioni, R., Sbrana, A., Zanella, E., 2002. Transport and deposition of pyroclastic density currents over an inhabited area : the deposits of the AD 79 eruption of Vesuvius at Herculaneum , Italy. Sedimentology 49, 929–953.
33. Gurioli, L., Houghton, B.F., Cashman, K.V., Cioni, R., 2005. Complex changes in eruption dynamics during the 79 AD eruption of Vesuvius. Bull. Volcanol. 67, 144–159. https://doi.org/10.1007/s00445-004-0368-4
34. Hammer, J.E., Rutherford, M.J., 2002. An experimental study of the kinetics of decompression-induced crystallization in silicic melt. J. Geophys. Res. Earth 107, 2021. https://doi.org/10.1029/2001jb000281
35. Higgins, M.D., 2000. Measurement of crystal size distributions. Am. Mineral. 85, 1105–1116.
36. Houghton, B.F., Wilson, C.J.N., 1989. A vesicularity index for pyroclastic deposits. Bull. Volcanol. 51, 451–462. https://doi.org/10.1007/BF01078811
37. Houghton, B.F., Wilson, C.J.N., Del Carlo, P., Coltelli, M., Sable, J.E., Carey, R.J., 2004. The influence of conduit processes on changes in style of basaltic Plinian eruptions: Tarawera 1886 and Etna 122 BC. J. Volcanol. Geotherm. Res. 137, 1–14. https://doi.org/10.1016/j.jvolgeores.2004.05.009
38. Hurwitz, S., Navon, O., 1994. Bubble nucleation in rhyolitic melts: Experiments at high pressure, temperature, and water content. Earth Planet. Sci. Lett. 122, 267–280. https://doi.org/10.1016/0012-821X(94)90001-9

39. Jaupart, C., Allegre, C.J., 1991. Gas Content, Eruption Rate and Instabilities of Eruption Regime in Silicic Volcanos. Earth Planet. Sci. Lett. 102, 413–429. https://doi.org/10.1016/0012-821x(91)90032-d

40. Joron, J.L., Metrich, N., Rosi, M., Santacroce, R., Sbrana, A., 1987. Chemistry and Petrography. In: Santacroce, R., (ed) Somma- Vesuvius. CNR Quad. Ric. Sci. 8 114, 105–174.

41. Klug, C., Cashman, K. V, Bacon, C.R., 2002. Structure and physical characteristics of pumice from the climactic eruption of Mount Mazama (Crater Lake), Oregon. Bull. Volcanol. 64, 486–501. https://doi.org/10.1007/s00445-002-0230-5

42. La Spina, G., Burton, M., de' Michieli Vitturi, M., Arzilli, F., 2016. Role of syn-eruptive plagioclase disequilibrium crystallization in basaltic magma ascent dynamics. Nat. Commun. 7, 13402. https://doi.org/10.1038/ncomms13402

43. Mader, H.M., Llewellin, E.W., Müller, S.P., 2013. The rheology of two-phase magmas: a review and analysis. J. Volcanol. Geotherm. Res. 257, 135–158. https://doi.org/10.1016/j.jvolgeores.2013.02.014

44. Marsh, B.D., 1988. Crystal size distribution (CSD) in rocks and the kinetics and dynamics of crystallization I. Theory. Contrib. to Mineral. Petrol. 99, 277–291.

45. Marzocchi, W., Sandri, L., Gasparini, P., Newhall, C.G., Boschi, E., 2004. Quantifying probabilities of volcanic events: The example of volcanic hazard at Mount Vesuvius. J. Geophys. Res. 109, B11201. https://doi.org/10.1029/2004JB003155

46. Massaro, S., Costa, A., Sulpizio, R., 2018. Evolution of the magma feeding system during a Plinian eruption: The case of Pomici di Avellino eruption of Somma–Vesuvius, Italy. Earth Planet. Sci. Lett. 482, 545–555. https://doi.org/10.1016/j.epsl.2017.11.030

47. Mastrolorenzo, G., Pappalardo, L., 2006. Magma degassing and crystallization processes during eruptions of high-risk Neapolitan-volcanoes: Evidence of common equilibrium rising processes in alkaline magmas. Earth Planet. Sci. Lett. 250, 164–181. https://doi.org/10.1016/j.epsl.2006.07.040

48. Mastrolorenzo, G., Palladino, D.M., Vecchio, G., Taddeucci, J., 2002. The 472 AD Pollena eruption of Somma-Vesuvius (Italy) and its environmental impact at the end of the Roman Empire. J. Volcanol. Geotherm. Res. 113, 19–36. https://doi.org/10.1016/S0377-0273(01)00248-7
49. Miyaji, N., Kan'no, A., Kanamaru, T., Mannen, K., 2011. High-resolution reconstruction of the Hoei eruption (AD 1707) of Fuji volcano, Japan. J. Volcanol. Geotherm. Res. 207, 113–129. https://doi.org/10.1016/j.jvolgeores.2011.06.013
50. Morgan, D.J., Jerram, D.A., 2006. On estimating crystal shape for crystal size distribution analysis. J. Volcanol. Geotherm. Res. 154, 1–7. https://doi.org/10.1016/j.jvolgeores.2005.09.016
51. Mueller, S.P., Scheu, B., Spieler, O., Dingwell, D.B., 2008. Permeability control on magma fragmentation. Geology 36, 399–402. http://doi.org/10.1130/G24605A.1
52. Noguchi, S., Toramaru, A., Shimano, T., 2006. Crystallization of microlites and degassing during magma ascent: Constraints on the fluid mechanical behavior of magma during the Tenjo Eruption on Kozu Island, Japan. Bull. Volcanol. 68, 432–449. https://doi.org/10.1007/s00445-005-0019-4
53. Pardo, N., Cronin, S.J., Wright, H.M.N., Schipper, C.I., Smith, I., Stewart, B., 2014. Pyroclast textural variation as an indicator of eruption column steadiness in andesitic Plinian eruptions at Mt. Ruapehu. Bull. Volcanol. 76, 1–19. https://doi.org/10.1007/s00445-014-0822-x
54. Pensa, A., Cas, R., Giordano, G., Porreca, M., Wallenstein, N., 2015. Transition from steady to unsteady Plinian eruption column: The VEI 5, 4.6 ka Fogo A Plinian eruption, São Miguel, Azores. J. Volcanol. Geotherm. Res. 305, 1–18. https://doi.org/10.1016/j.jvolgeores.2015.09.012
55. Pistolesi, M., Bertagnini, A., Di Roberto, A., Isaia, R., Vona, A., Cioni, R., Giordano, G., 2017. The Baia–Fondi di Baia eruption at Campi Flegrei: stratigraphy and dynamics of a multi-stage caldera reactivation event. Bull. Volcanol. 79, 67. https://doi.org/10.1007/s00445-017-1149-1
56. Polacci, M., Papale, P., Rosi, M., 2001. Textural heterogeneities in pumices from the climactic eruption of Mount Pinatubo, 15 June 1991, and implications for

magma ascent dynamics. Bull. Volcanol. 63, 83–97. https://doi.org/10.1007/s004450000123

57. Polacci, M., Baker, D.R., Mancini, L., Tromba, G., Zanini, F., 2006. Three-dimensional investigation of volcanic textures by X-ray microtomography and implications for conduit processes. Geophys. Res. Lett. 33, L13312. https://doi.org/10.1029/2006GL026241
58. Rolandi, G., Munno, R., Postiglione, I., 2004. The A.D. 472 eruption of the Somma volcano. J. Volcanol. Geotherm. Res. 129, 291–319. https://doi.org/10.1016/S0377-0273(03)00279-8
59. Romano, C., Giordano, D., Papale, P., Mincione, V., Dingwell, D.B., Rosi, M., 2003. The dry and hydrous viscosities of alkaline melts from Vesuvius and Phlegrean Fields. Chem. Geol. 202, 23–38. https://doi.org/10.1016/s0009-2541(03)00208-0
60. Romano, C., Vona, A., Campagnola, S., Giordano, G., Arienzo, I., Isaia, R., 2020. Modelling and physico-chemical constraints to the 4.5 ka Agnano-Monte Spina Plinian eruption (Campi Flegrei, Italy). Chem. Geol. 532, 119301. https://doi.org/10.1016/j.chemgeo.2019.119301
61. Rosi, M., Santacroce, R., 1983. The A.D. 472 "Pollena" eruption: volcanological and petrological data for this poorly-known, Plinian-type event at Vesuvius. J. Volcanol. Geotherm. Res. 17, 249–271. https://doi.org/10.1016/j.jvolgeores.2008.06.025
62. Saar, M.O., Manga, M., 1999. Permeability-porosity relationship in vesicular basalts. Geophys. Res. Lett. 26, 111–114.
63. Sable, J.E., Houghton, B.F., Del Carlo, P., Coltelli, M., 2006. Changing conditions of magma ascent and fragmentation during the Etna 122 BC basaltic Plinian eruption: Evidence from clast microtextures. J. Volcanol. Geotherm. Res. 158, 333–354. https://doi.org/10.1016/j.jvolgeores.2006.07.006
64. Sahagian, D., Proussevitch, A.A., 1998. 3D particle size distributions from 2D observations: stereology for natural applications. J. Volcanol. Geotherm. Res. 84, 173–196. https://doi.org/10.1016/S0377-0273(98)00043-2

65. Santacroce, R., Cioni, R., Marianelli, P., Sbrana, A., Sulpizio, R., Zanchetta, G., Donahue, D.J., Joron, J.L., 2008. Age and whole rock-glass compositions of proximal pyroclastics from the major explosive eruptions of Somma-Vesuvius: A review as a tool for distal tephrostratigraphy. J. Volcanol. Geotherm. Res. 177, 1–18. https://doi.org/10.1016/j.jvolgeores.2008.06.009

66. Scaillet, B., Pichavant, M., Cioni, R., 2008. Upward migration of Vesuvius magma chamber over the past 20,000 years. Nature 455, 216–219. https://doi.org/10.1038/nature07232

67. Scandone, R., Malone, S.D., 1985. Magma supply, magma discharge and readjustment of the feeding system of mount St. Helens during 1980. J. Volcanol. Geotherm. Res. 23, 239–262. https://doi.org/10.1016/0377-0273(85)90036-8

68. Shea, T., Hammer, J.E., 2013. Kinetics of cooling- and decompression-induced crystallization in hydrous mafic-intermediate magmas. J. Volcanol. Geotherm. Res. 260, 127–145. https://doi.org/10.1016/j.jvolgeores.2013.04.018

69. Shea, T., Larsen, J.F., Gurioli, L., Hammer, J.E., Houghton, B.F., Cioni, R., 2009. Leucite crystals: Surviving witnesses of magmatic processes preceding the 79AD eruption at Vesuvius, Italy. Earth Planet. Sci. Lett. 281, 88–98. https://doi.org/10.1016/j.epsl.2009.02.014

70. Shea, T., Gurioli, L., Larsen, J.F., Houghton, B.F., Hammer, J.E., Cashman, K. V, 2010a. Linking experimental and natural vesicle textures in Vesuvius 79AD white pumice. J. Volcanol. Geotherm. Res. 192, 69–84. https://doi.org/10.1016/j.jvolgeores.2010.02.013

71. Shea, T., Houghton, B.F., Gurioli, L., Cashman, K. V, Hammer, J.E., Hobden, B.J., 2010b. Textural studies of vesicles in volcanic rocks: An integrated methodology. J. Volcanol. Geotherm. Res. 190, 271–289. https://doi.org/10.1016/j.jvolgeores.2009.12.003

72. Shea, T., Gurioli, L., Houghton, B.F., Cioni, R., Cashman, K. V, 2011. Column collapse and generation of pyroclastic density currents during the A.D. 79 eruption of Vesuvius: The role of pyroclast density. Geology 39, 695–698. https://doi.org/10.1130/G32092.1

73. Shea, T., Gurioli, L., Houghton, B.F., 2012. Transitions between fall phases and pyroclastic density currents during the AD 79 eruption at Vesuvius: building a transient conduit model from the textural and volatile record. Bull. Volcanol. 74, 2363–2381. https://doi.org/10.1007/s00445-012-0668-z

74. Shea, T., Hellebrand, E., Gurioli, L., Tuffen, H., 2014. Conduit- to Localized-scale Degassing during Plinian Eruptions: Insights from Major Element and Volatile (Cl and H2O) Analyses within Vesuvius AD 79 Pumice. J. Petrol. 55, 315–344. https://doi.org/10.1093/petrology/egt069

75. Sigurdsson, H., Cornell, W., Carey, S., 1990. Influence of magma withdrawal on composi- tional gradients during the AD 79 Vesuvius eruption. Nature 345, 519–521. https://doi.org/10.1016/0021-9797(80)90501-9

76. Sulpizio, R., Mele, D., Dellino, P., La Volpe, L., 2005. A complex, Subplinian-type eruption from low-viscosity, phonolitic to tephri-phonolitic magma: the AD 472 (Pollena) eruption of Somma-Vesuvius, Italy. Bull. Volcanol. 67, 743–767. https://doi.org/10.1007/s00445-005-0414-x

77. Sulpizio, R., Mele, D., Dellino, P., La Volpe, L., 2007. Deposits and physical properties of pyroclastic density currents during complex Subplinian eruptions: the AD 472 (Pollena) eruption of Somma-Vesuvius, Italy. Sedimentology 54, 607–635. https://doi.org/10.1111/j.1365-3091.2006.00852.x

78. Szramek, L.A., 2016. Mafic Plinian eruptions: Is fast ascent required? J. Geophys. Res. Solid Earth 121, 7119–7136. https://doi.org/10.1002/2016JB013208

79. Toramaru, A., 1995. Numerical study of nucleation and growth of bubbles in viscous magmas. J. Geophys. Res. 100, 1913–1931.

80. Trolese, M., Cerminara, M., Esposti Ongaro, T., Giordano, G., 2019. The footprint of column collapse regimes on pyroclastic flow temperatures and plume heights. Nat. Commun. 10. https://doi.org/10.1038/s41467-019-10337-3

81. Vona, A., Romano, C., Dingwell, D.B., Giordano, D., 2011. The rheology of crystal-bearing basaltic magmas from Stromboli and Etna. Geochim. Cosmochim. Acta 75, 3214–3236. https://doi.org/10.1016/j.gca.2011.03.031

82. Vona, A., Romano, C., Giordano, D., Russell, J.K., 2013. The multiphase rheology of magmas from Monte Nuovo (Campi Flegrei, Italy). Chem. Geol. 346, 213–227. https://doi.org/10.1016/j.chemgeo.2012.10.005
83. Vona, A., Ryan, A.G., Russell, J.K., Romano, C., 2016. Models for viscosity and shear localization in bubble-rich magmas. Earth Planet. Sci. Lett. 449, 26–38. https://doi.org/10.1016/j.epsl.2016.05.029
84. Vona, A., Di Piazza, A., Nicotra, E., Romano, C., Viccaro, M., Giordano, G., 2017. The complex rheology of megacryst-rich magmas: The case of the mugearitic "cicirara" lavas of Mt. Etna volcano. Chem. Geol. 458, 48–67. https://doi.org/10.1016/j.chemgeo.2017.03.029
85. Wilson, L., Sparks, R.S.J., Walker, G.P.L., 1980. Explosive volcanic eruptions - IV. The control of magma properties and conduit geometry on eruption column behaviour. Geophys. J. R. Astron. Soc. 63, 117–148.
86. Wylie, J.J., Voight, B., Whitehead, J.A., 1999. Instability of Magma Flow from Volatile-Dependent Viscosity. Science 285, 1883–1885.

Table and Figure Captions

Tab. 1. Summary of textural features of the juvenile clasts from Pollena eruption deposits.

Fig. 1. Stratigraphy and chemistry of the 472 CE Pollena eruption of Vesuvius. (A) Location map of Vesuvius band distribution of the fall deposits, expressed as 10 cm isopach of each fall bed (from Sulpizio et al., 2005). Black circle indicates the inferred vent location; star locates sampling site (VS7 section). (B-C) Composite stratigraphic section of the Pollena eruption (B) and VS7 section (C) (both redrawn from Sulpizio et al., 2005). In (B), the three main phases of the eruption are reported in the left column. In (C), the colored circles indicate fall beds sampled for textural characterization. (D) TAS (Total Alkali vs. Silica) diagram showing the bulk rock composition of Pollena products (data from Sulpizio et al., 2005, colored symbols; and from Santacroce et al., 2008, dark grey

field). Bulk chemistry of 79 CE Pompei eruption products is also reported as a light grey field (Santacroce et al., 2008). (E) Grain size distribution of fall deposits from VS7 section.

Fig. 2. Stratigraphical variation of textural features of Pollena eruption fall products (L1-L8). (A) Density (g cm^{-3}) and porosity (vol.%) distributions of the fall beds of Pollena eruption. Stars indicate characteristic density/porosity classes selected for VSD and CSD analyses. (B) Bulk porosity (%) vs. pore connectivity. Blue circles indicate raw data; red boxes confine the 25^{th} and 75^{th} percentiles of both connectivity and porosity distributions. (C) Vesicle Number Density (mm^{-3}). All analyzed clasts (empty symbols) and mean values from clasts of modal density (MD) (filled symbols) are displayed. (D) Crystal contents (%) referred to the solid rock. (E) Crystal Number Density (mm^{-2}). Mean values are plotted as filled symbols.

Fig. 3. Comparison of connected porosity and bulk porosity. Solid lines describe 1:1 relation (no isolated porosity). Dashed lines show contours of the volume percentage of isolated vesicles, labeled in (A).

Fig. 4. Results of textural analysis on representative clasts from L1 bed (A-C) and L8T bed (D-F). In (A) and (D), BSE images acquired at 20x (top), 80x (middle) and 320 x (bottom) are reported. (B,E) Vesicle volume distributions of juveniles from L1 bed (B) and L8T bed (E). (C,F) Crystal area distributions of juveniles from L1 bed (C) and L8T bed (F).

Fig. 5. Cumulative Vesicle Volume Distribution (CVVD). In each diagram, data from all clasts are plotted as gray curves in the background to facilitate comparison among the samples. (A) Comparison among different key stratigraphic layers. (B-H) Vesicle population variability within each layer.

Fig. 6. Cumulative Crystal Volume Distribution (CCVD) of the analyzed stratigraphic layers L1 (A-C), L2-3 (D-F), L4 (G-I), L5-7 (J-L), and L8 (M-O). In each diagram, data

from all clasts are plotted as gray curves in the background to facilitate comparison among the samples.

Fig. 7. (A) Variation of Crystal Size Distribution (CSD) parameters (slope and intercept) determined by linear regression of the crystal populations (Tab. 1 and Appendix 1). Clinopyroxene CSDs have been modeled using two linear segments, for microphenocryst (> 100 μm) and microlite (< 30 μm) populations. (B) Crystallinity vs. Crystal Number Density (CND) of leucite and clinopyroxene.

Fig. 8. Crystallization timescales of leucite and clinopyroxene (microphenocrysts: > 100 μm; microlites: < 30 μm). Timescales [$\tau = -1/(G \times slope_{CSD})$] were estimated using CSD slopes (Tab. 1) and a range of experimentally derived growth rates G. Leucite: $G_{lc(min)}$ = $2x10^{-8}$ mm s^{-1}; $G_{lc(max)}$ = $1x10^{-7}$ mm s^{-1} (Shea et al., 2009). Clinopyroxene: $G_{cpx(min)}$ = $2x10^{-6}$ mm s^{-1} (Shea and Hammer, 2013); $G_{cpx(max)}$ = $2x10^{-5}$ mm s^{-1} (Arzilli et al., 2019a).

Fig. 9. Comparison of crystallinity and porosity. Porosity values are referred to the bulk sample (A) and to the melt phase alone (B). Crystallinity is expressed on a vesicle-free basis in both diagrams.

Fig. 10. Stratigraphic variation of (A) Mass Discharge Rates (MDR) calculated by Sulpizio et al. (2005) on the basis of field analysis of pyroclast dispersion and (B) effect of crystals on magma rheology expressed as relative viscosity ($\eta_r = \eta_{L+C} / \eta_L$) and calculated in this study on the basis of crystal textures using the formulation of Vona et al. (2011).

Fig. 11. Rheological modeling (A) and relation with field-derived MDRs (B). Dashed lines in (A) describe the T dependence of the viscosity of pure liquid calculated on chemical basis using the GRD model (Giordano et al., 2008) and bulk compositions of Sulpizio et al. (2005). Solid lines include the effect of crystals according to the equation by Vona et al. (2011) (see Fig. 9). Black circles in (A) indicate the syn-eruptive variation of the two-phase (liquid+crystals) magma viscosity assuming T = 850 °C for L1 magma (blue lines), T =

1050 °C for L8 magma (red lines) and assuming a linear gradient for intermediate eruptive units (e.g., Cioni et al., 1998).

Fig. 12. Schematic diagram summarizing the main changes in the dynamics of Pollena eruption. (A) Phonolite magma (L1) is first erupted from the apical part of the reservoir. (B) Lateral textural gradients induced by differential ascent velocity (red arrows) modulate eruption energy (outgassing ability) during L2, L4, L6 and L7 events. While L2 and L4 events conclude with the deposition of an ash layer, magma densification in L7 ultimately leads to the column collapse and disruption of the upper conduit system concluding Phase I. (C) Sustained column restores after a short stasis at L3, L5, and L8 events, in response to clearing of the outgassed crystal-rich and high-viscosity magmas.

Tab. 1. Su

Clast ID	Unit	Density Class	Density ρ (kg m^{-3})	Porosity ϕ_{ves} (vol%)	VND [a] (mm^{-3})	Median Vesicle Size (μm)	Cristallinity ϕ_{xls} (vol%)	Leucite (vol%) [b]			Median Leucite Size (μm)	Leucite CND (mm^{-3})	Leucite CSD slope (mm^{-1})	Leucite CSD intercept (mm^{-1})	Pyroxene (vol%) [b]			
								ϕ_{lc}	ϕ_{lc_m}	ϕ_{lc_mp}					ϕ_{px}	ϕ_{px_m}	ϕ_{px_mp}	ϕ_{px_p}
L1_72	L1	LD	709	72	3.34E+05	70	-	-	-	-	-	-			-	-	-	-
L1_2	L1	MD	1112	57	2.05E+05	50	25.3	19.4	19.1	0.3	55	4.37E+03	-66.9	13.53	5.9	3.0	1.2	1.7
L1_20	L1	MD	1155	55	1.65E+05	45	20.6	17.0	17.0	0.0	35	6.29E+03	-102	15.06	3.7	3.2	0.0	0.4
L1_82	L1	HD	1557	39	3.74E+05	25	-	-	-	-	-	-			-	-	-	-
L2_24	L2	M1D	1107	57	1.89E+05	105	33.2	25.5	25.5	0.0	35	2.22E+04	-102	15.16	7.7	2.2	1.7	3.8
L2_15	L2	M2D	1451	44	2.86E+05	60	28.0	18.8	18.8	0.0	30	2.47E+04	-102	15.15	9.2	3.1	0.2	5.9
L3_79	L3	LD	943	63	2.71E+05	80	-	-	-	-	-	-			-	-	-	-
L3_2	L3	MD	1281	50	3.08E+05	105	43.5	29.8	29.8	0.0	25	5.18E+04	-121	16.17	13.8	7.4	0.9	5.4
L3_9	L3	MD	1229	52	1.35E+05	105	40.7	29.2	29.2	0.0	35	2.63E+04	-94	15.32	11.5	9.2	0.8	1.5
L3_28	L3	HD	1654	36	6.20E+05	70	-	-	-	-	-	-			-	-	-	-
L4B_98	L4 Bottom	LD	934	64	3.20E+05	85	-	-	-	-	-	-			-	-	-	-
L4B_35	L4 Bottom	MD	1241	52	1.72E+05	90	26.8	14.8	14.8	0.0	15	8.24E+04	-195	17.38	12.0	7.5	1.7	2.8
L4B_55	L4 Bottom	MD	1249	51	1.54E+05	80	33.6	24.3	24.3	0.0	[illegible]	[illegible]7E+04	-153	17.02	9.4	7.5	1.6	0.2
L4B_97	L4 Bottom	HD	1717	33	4.21E+05	50	-	-	-	-	-	-			-	-	-	-
L4M_21	L4 Middle	LD	842	67	6.66E+05	105	-	-	-	-	-	-			-	-	-	-
L4M_7	L4 Middle	MD	1083	58	2.13E+05	70	39.0	22.7	22.7	0.0	15	6.07E+04	-188	17.82	16.3	5.8	0.5	10.0
L4M_29	L4 Middle	MD	1020	60	2.61E+05	70	30.7	20.7	20.7	0.0	15	5.43E+04	-175	17.36	10.0	6.3	0.8	2.9
L4M_40	L4 Middle	HD	1323	49	2.90E+05	60	-	-	-	-	-	-			-	-	-	-
L4T_28	L4 Top	LD	927	64	9.97E+05	100	-	-	-	-	-	-			-	-	-	-
L4T_54	L4 Top	MD	1278	50	7.05E+05	60	26.5	13.2	[illegible]	0.0	15	4.49E+04	-208	17.57	13.4	6.8	0.2	6.3
L4T_67	L4 Top	MD	1273	50	2.95E+05	60	46.2	28.6	[illegible]	0.0	15	4.72E+04	-177	17.73	17.6	12.1	0.7	4.8
L4T_23	L4 Top	HD	1521	41	4.41E+05	70	-	-	-	-	-	-			-	-	-	-
L5_79	L5	LD	1024	60	6.17E+05	50	-	-	-	-	-	-			-	-	-	-
L5_1	L5	MD	1520	41	6.15E+05	50	[illegible]	22.8	22.8	0.0	15	3.50E+04	-154	17.18	13.1	9.9	1.0	2.2
L5_3	L5	MD	1572	39	4.49E+05	40	[illegible]	24.9	24.9	0.0	15	4.75E+04	-166	17.40	16.5	9.7	2.6	4.2
L5_13	L5	HD	1846	28	7.14E+05	35	-	-	-	-	-	-			-	-	-	-
L6_82	L6	LD	723	72	5.27E+05	55	-	-	-	-	-	-			-	-	-	-
L6_5	L6	MD	1070	58	1.90E+05	[illegible]	45.9	31.9	31.9	0.0	25	3.95E+04	-120	16.32	13.9	8.5	2.6	2.8
L6_41	L6	MD	1008	61	1.54E+05	70	36.2	27.5	27.5	0.0	20	4.66E+04	-141	16.67	8.7	6.0	2.2	0.5
L6_49	L6	HD	1763	31	5.92E+0[illegible]	3[illegible]	-	-	-	-	-	-			-	-	-	-
L7_3	L7	LD	1002	61	2.6[illegible]E+05	95	-	-	-	-	-	-			-	-	-	-
L7_49	L7	MD	1264	51	1.77[illegible]05	75	43.9	32.8	32.8	0.0	25	2.99E+04	-145	16.97	11.0	7.3	2.0	1.8
L7_98	L7	MD	1220	53	3.48[illegible]+05	50	45.7	33.6	33.6	0.0	25	5.09E+04	-115	16.71	12.1	8.3	2.5	1.3
L7_11	L7	HD	1639	36	1.36E+05	80	-	-	-	-	-	-			-	-	-	-
L8B_16	L8 Bottom	LD	1102	60	2.48E+05	85	-	-	-	-	-	-			-	-	-	-
L8B_1	L8 Bottom	MD	1264	54	2.51E+05	50	45.9	26.2	26.2	0.0	20	9.38E+04	-140	17.10	19.7	7.5	3.1	9.1
L8B_2	L8 Bottom	MD	1368	50	1.82E+05	70	48.6	25.3	25.3	0.0	20	7.34E+04	-169	17.45	23.3	10.2	2.6	10.6
L8B_41	L8 Bottom	HD	1553	44	2.56E+05	80	-	-	-	-	-	-			-	-	-	-
L8T_81	L8 Top	LD	1161	58	1.03E+05	105	-	-	-	-	-	-			-	-	-	-
L8T_5	L8 Top	MD	1459	47	6.85E+04	95	54.6	30.8	30.3	0.5	25	5.40E+04	-118	16.61	23.8	17.6	0.7	5.5
L8T_25	L8 Top	MD	1480	46	9.78E+04	65	45.6	28.8	28.8	0.0	20	3.42E+05	-222	18.54	16.8	8.1	1.9	6.8
L8T_27	L8 Top	HD	1645	40	3.11E+05	60	-	-	-	-	-	-			-	-	-	-

[a] Recalculated with reference to the melt alone (Nv^{corr} in Shea et al., 2010); [b] Subscripts are: m = microlites (L < 100 μm); mp = microphenocrysts (100 < L < 300 μm); p = phenocrysts (L > 300 μm).

Declaration of interests

☒ The authors declare that they have no known competing financial interests or personal relationships that could have appeared to influence the work reported in this paper.

☐The authors declare the following financial interests/personal relationships which may be considered as potential competing interests:

Highlights:

- A subplinian eruption is a reference scenario in case of Vesuvius reactivation
- Pyroclast textures are used to reconstruct Pollena subplinian eruption dynamics
- Conduit processes control eruption intensity and fall/PDC transition
- Subplinian and Plinian events at Vesuvius show similar eruptive mechanisms

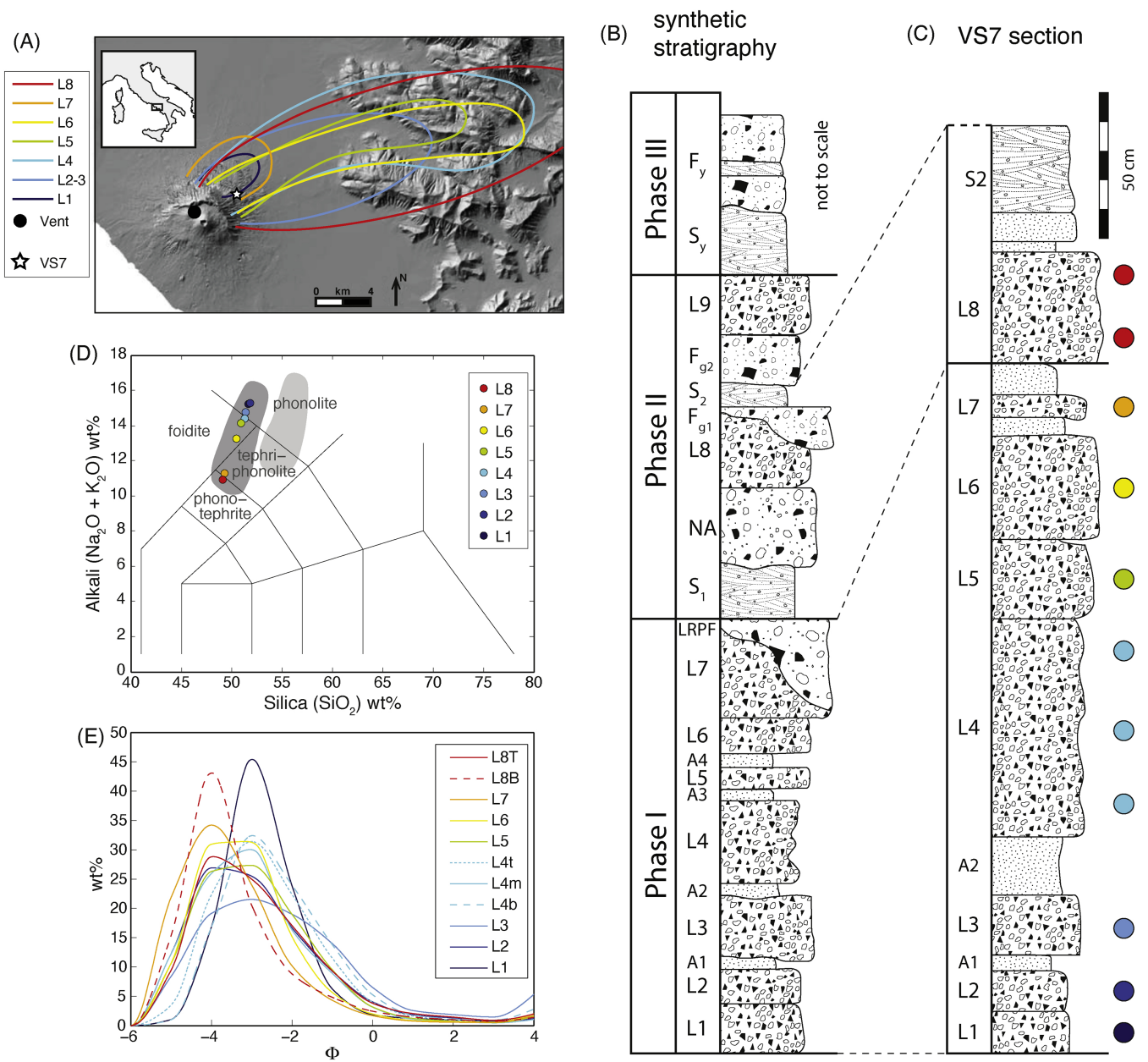
(A)
L8
L7
L6
L5
L4
L2-3
L1
Vent
VS7
0 km 4
N
(B) synthetic stratigraphy
(C) VS7 section
not to scale
50 cm
Phase III
Phase II
Phase I
Fy
Sy
L9
Fg2
S2
Fg1
L8
NA
S1
LRPF
L7
L6
A4
L5
A3
L4
A2
L3
A1
L2
L1
(D)
Alkali (Na2O + K2O) wt%
Silica (SiO2) wt%
foidite
phonolite
tephri–phonolite
phono–tephrite
(E)
wt%
Φ
L8T
L8B
L4t
L4m
L4b

Figure 1

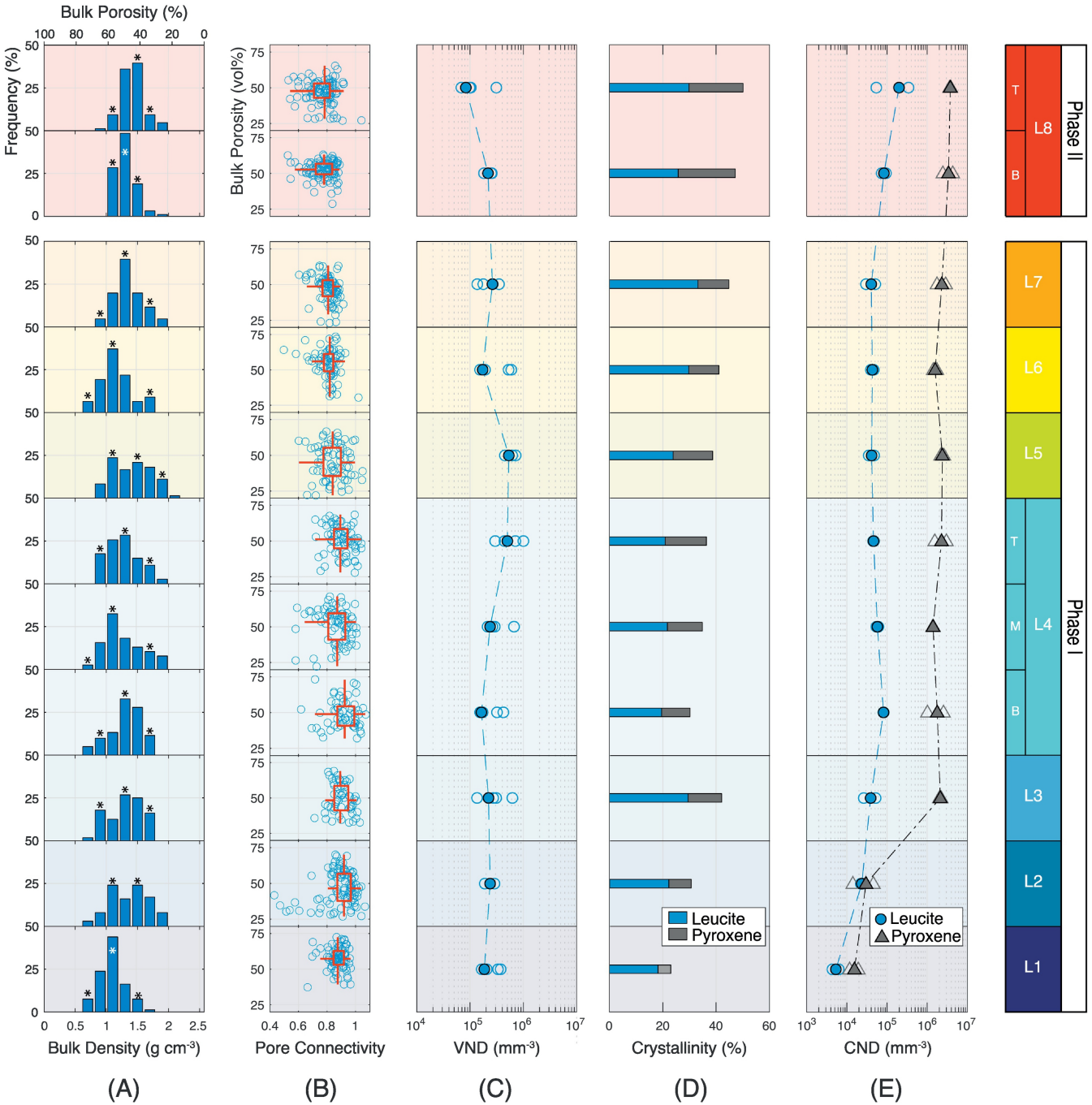
Bulk Porosity (%)
Frequency (%)
Bulk Porosity (vol%)
Phase II
L8
T
B
L7
L6
L5
Phase I
L4
M
L3
L2
L1
Leucite
Pyroxene
Bulk Density (g cm-3)
Pore Connectivity
VND (mm-3)
Crystallinity (%)
CND (mm-3)
(A)
(B)
(C)
(D)
(E)

Figure 2

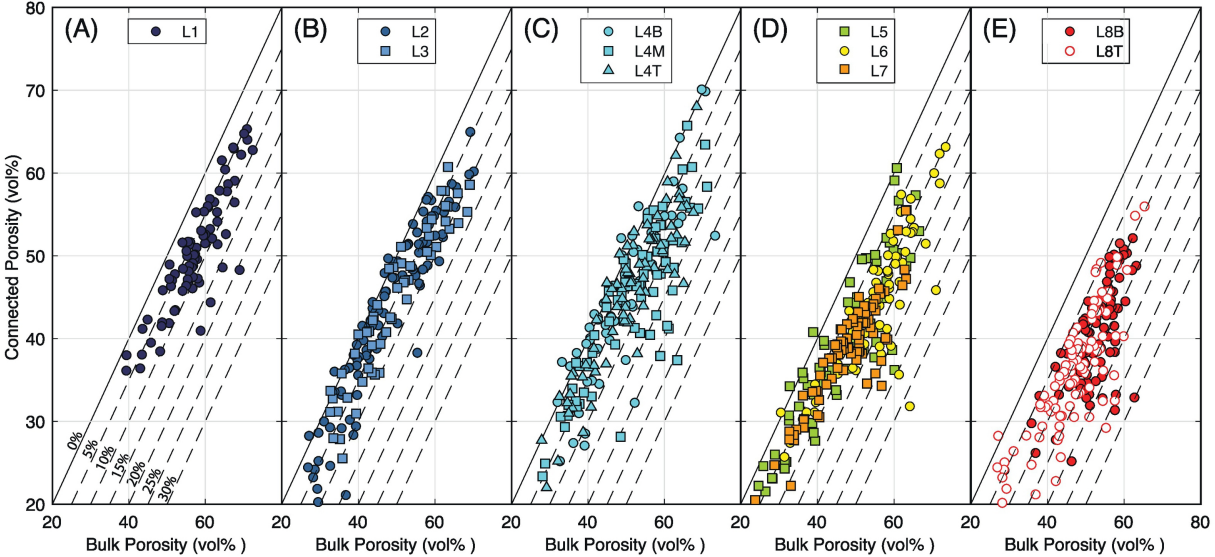
(A)
L1
(B)
L2
L3
(C)
L4B
L4M
L4T
(D)
L5
L6
L7
(E)
L8B
L8T
Connected Porosity (vol%)
Bulk Porosity (vol%)
0%
5%
10%
15%
20%
25%
30%

Figure 3

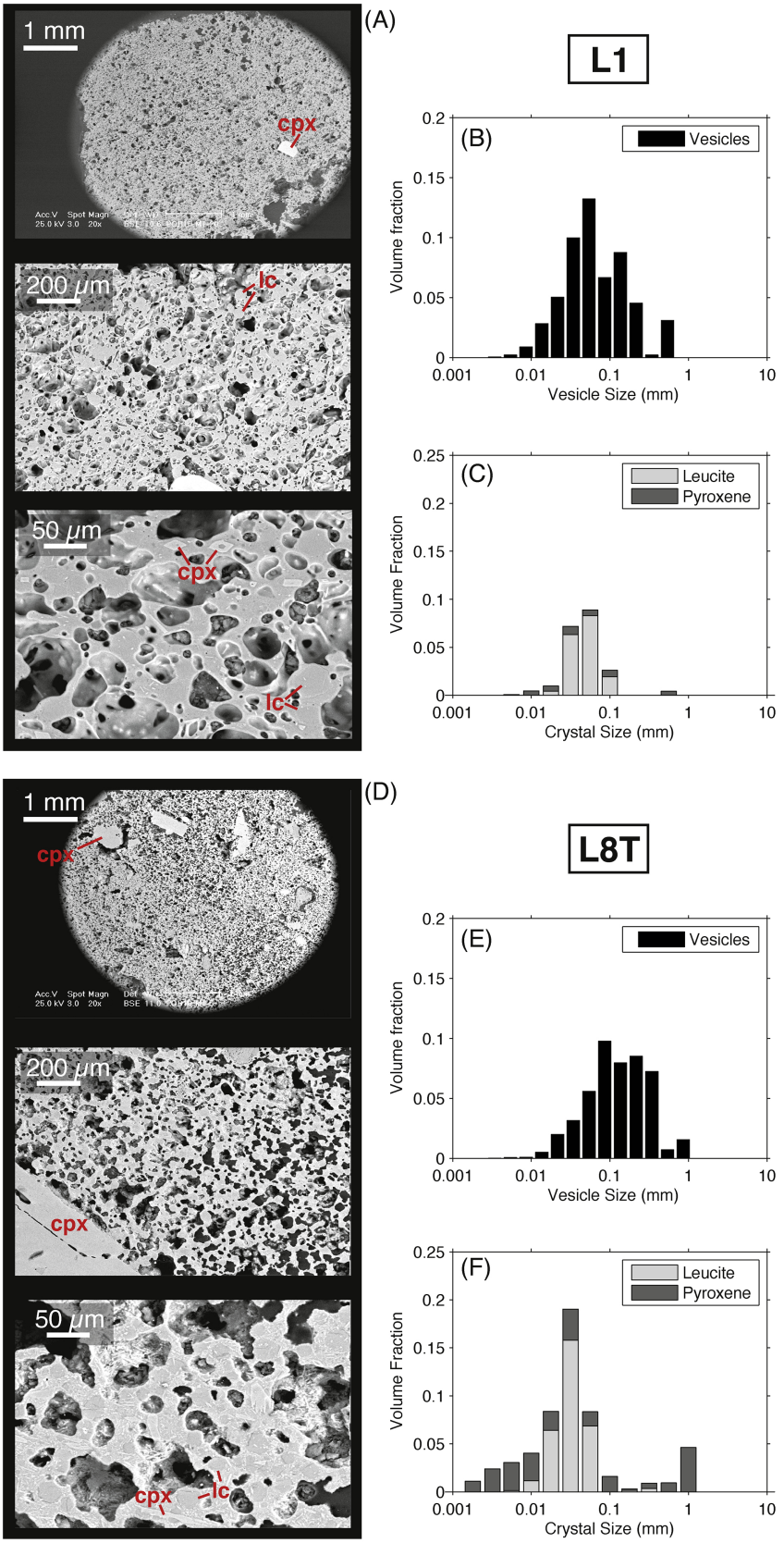
(A)
1 mm
cpx
200 μm
lc
50 μm
cpx
lc
L1
(B)
Vesicles
Volume fraction
Vesicle Size (mm)
(C)
Leucite
Pyroxene
Volume Fraction
Crystal Size (mm)
(D)
1 mm
cpx
200 μm
cpx
50 μm
cpx
lc
L8T
(E)
Vesicles
Volume fraction
Vesicle Size (mm)
(F)
Leucite
Pyroxene
Volume Fraction
Crystal Size (mm)

Figure 4

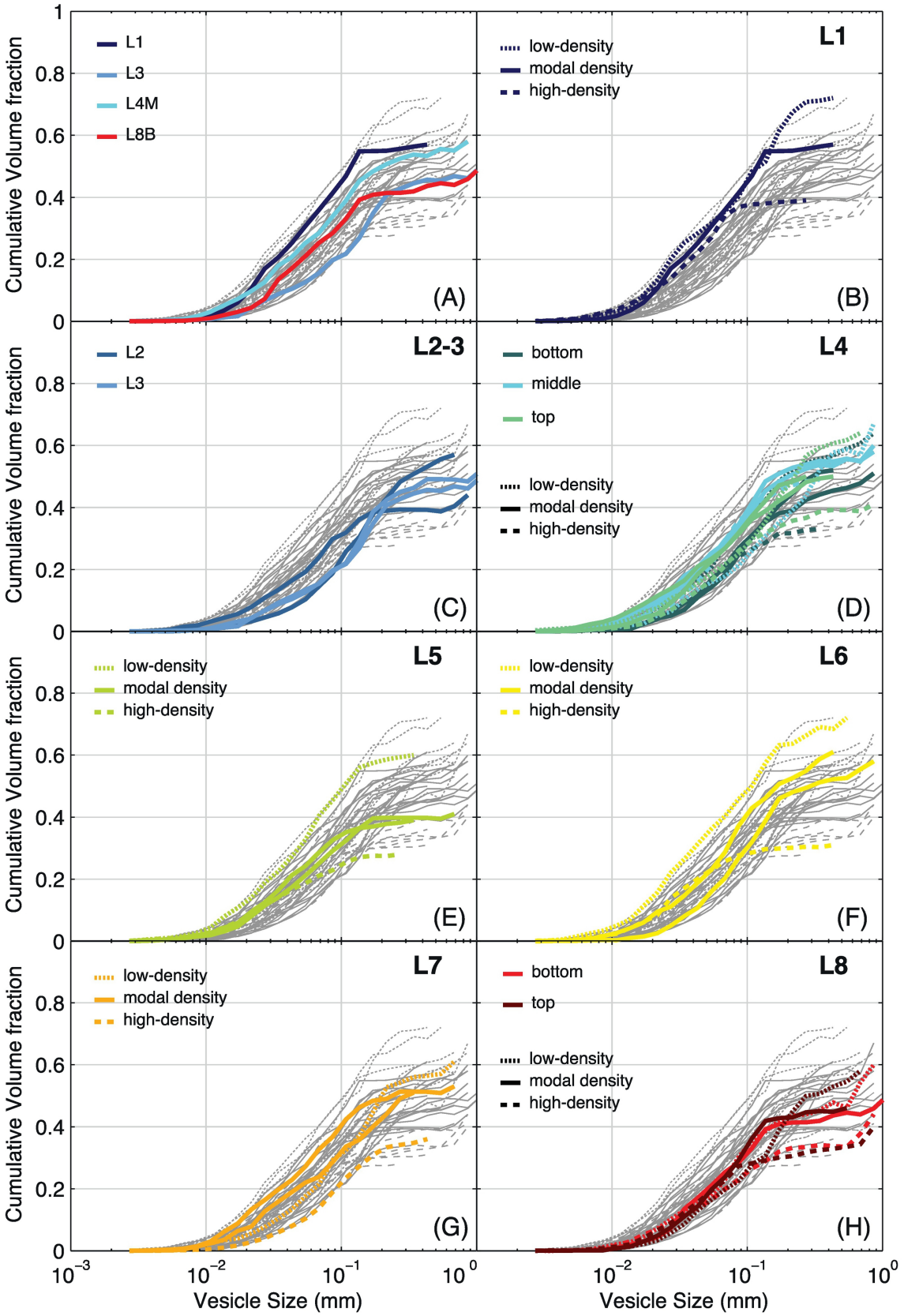
Cumulative Volume fraction
Vesicle Size (mm)
L1
L3
L4M
L8B
(A)
low-density
modal density
high-density
L1
(B)
L2
L3
L2-3
(C)
bottom
middle
top
low-density
modal density
high-density
L4
(D)
low-density
modal density
high-density
L5
(E)
low-density
modal density
high-density
L6
(F)
low-density
modal density
high-density
L7
(G)
bottom
top
low-density
modal density
high-density
L8
(H)

Figure 5

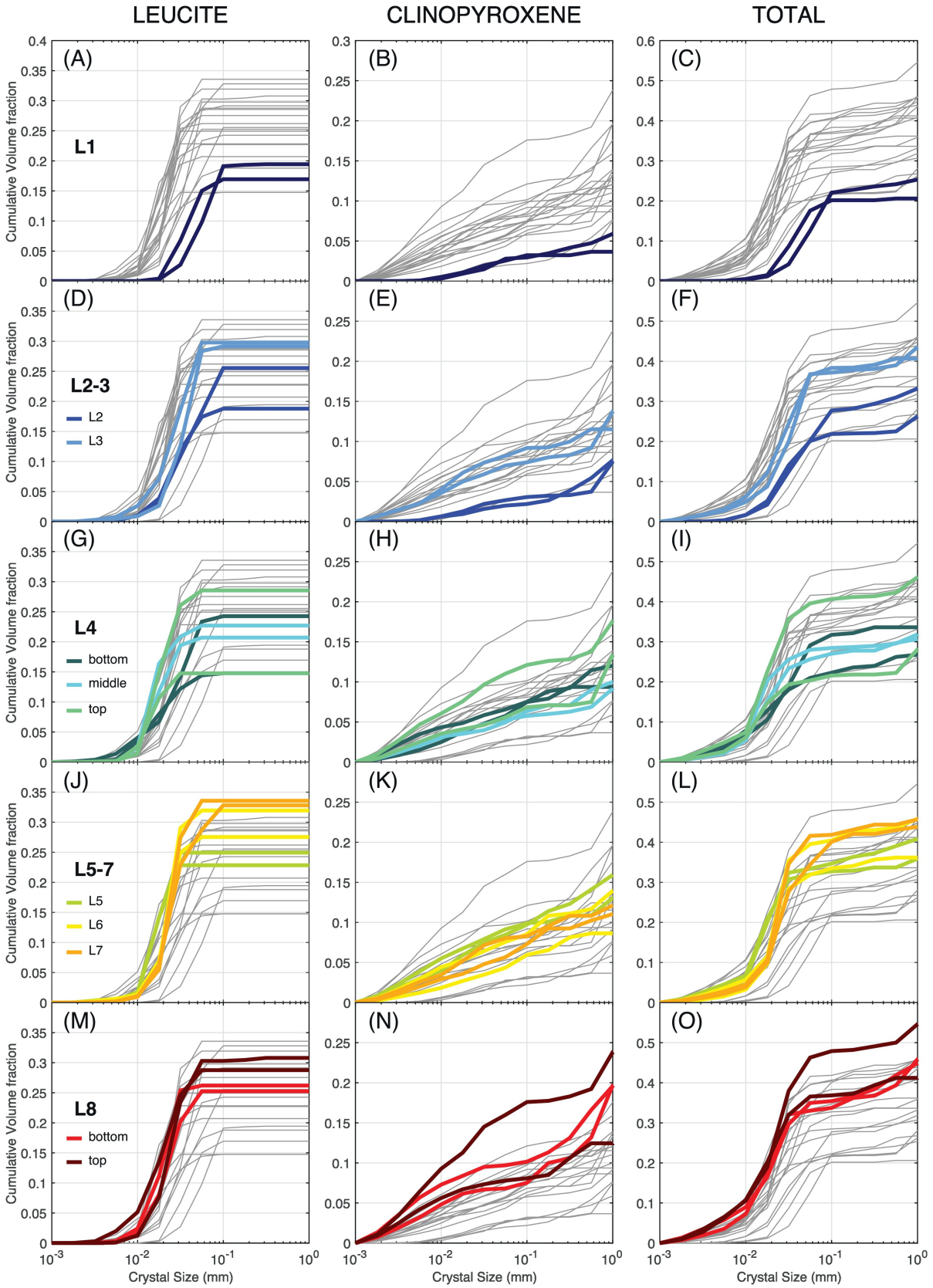
LEUCITE
CLINOPYROXENE
TOTAL
(A)
(B)
(C)
L1
(D)
(E)
(F)
L2-3
L2
L3
(G)
(H)
(I)
L4
bottom
middle
top
(J)
(K)
(L)
L5-7
L5
L6
L7
(M)
(N)
(O)
L8
bottom
top
Cumulative Volume fraction
Crystal Size (mm)

Figure 6

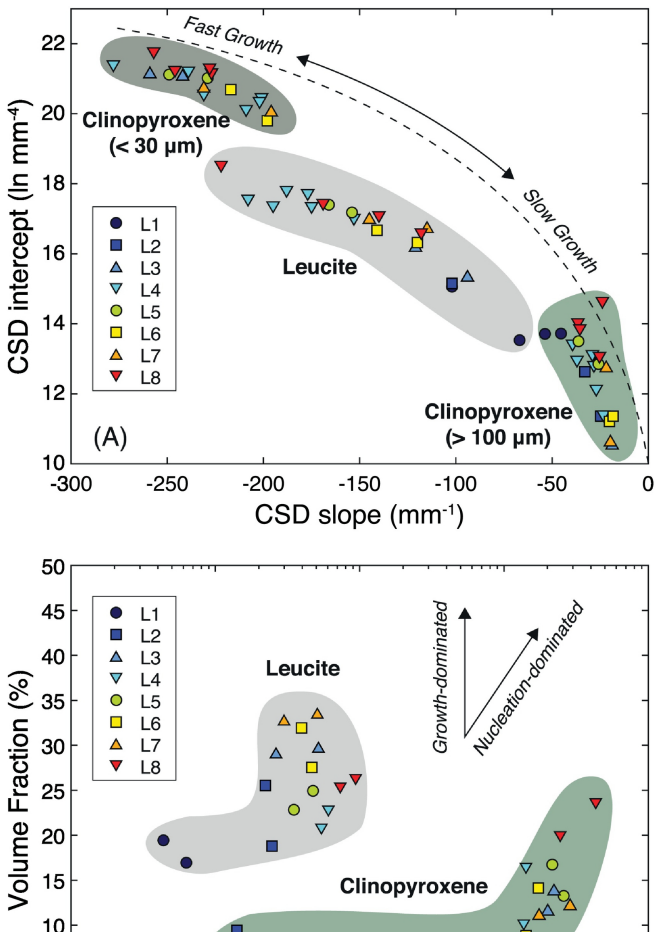
Fast Growth
Slow Growth
Clinopyroxene
(< 30 µm)
Leucite
Clinopyroxene
(> 100 µm)
L1
L2
L3
L4
L5
L6
L7
L8
(A)
CSD intercept (ln mm⁻⁴)
CSD slope (mm⁻¹)
22
20
18
16
14
12
10
-300
-250
-200
-150
-100
-50
0

Leucite
Clinopyroxene
Growth-dominated
Nucleation-dominated
L1
L2
L3
L4
L5
L6
L7
L8
(B)
Volume Fraction (%)
Crystal Number Density, N_V (mm⁻³)
50
45
40
35
30
25
20
15
10
5
0
10³
10⁴
10⁵
10⁶
10⁷

Figure 7

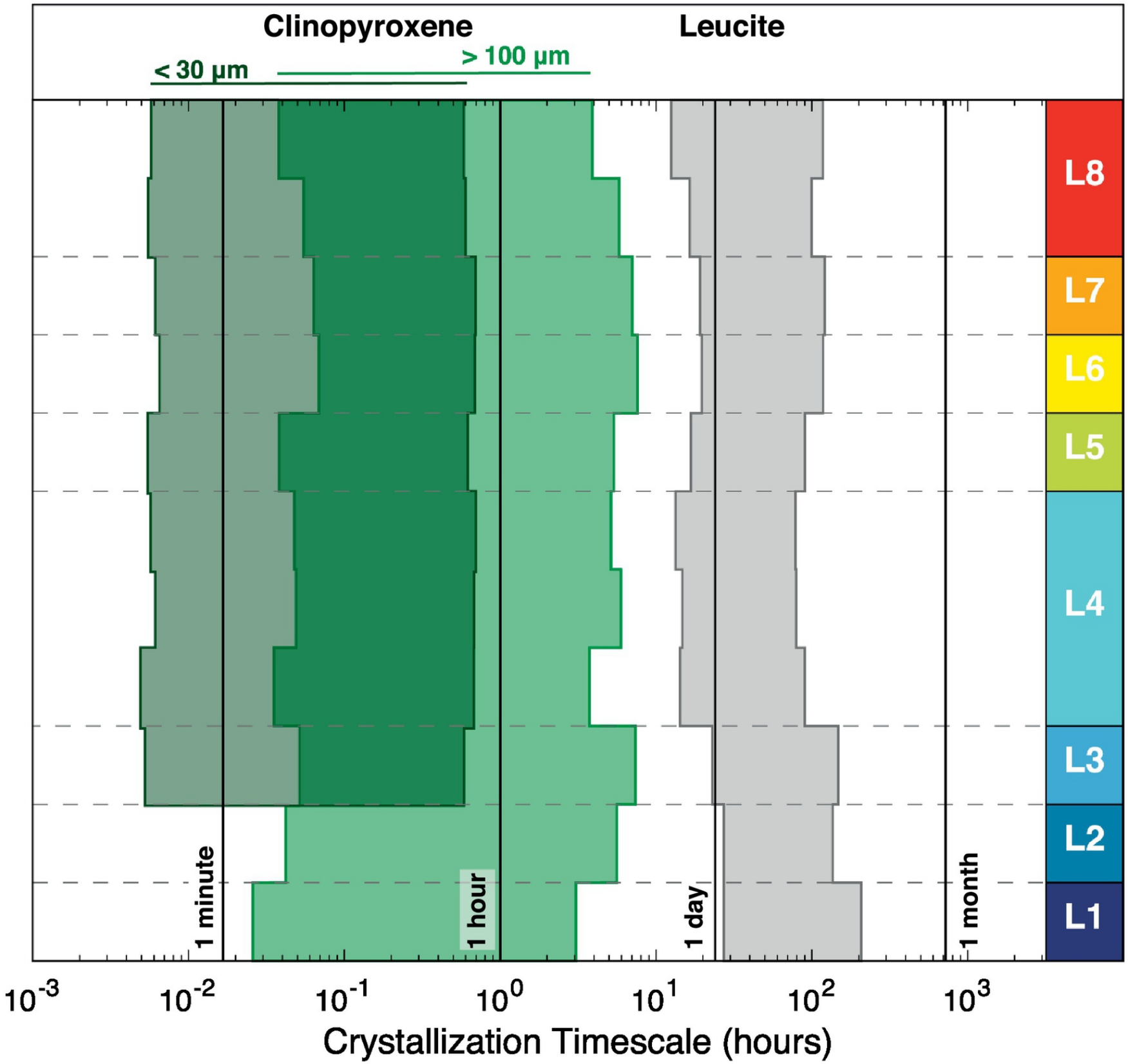
Clinopyroxene
Leucite
< 30 µm
> 100 µm
L8
L7
L6
L5
L4
L3
L2
L1
1 minute
1 hour
1 day
1 month
10-3
10-2
10-1
100
101
102
103
Crystallization Timescale (hours)

Figure 8

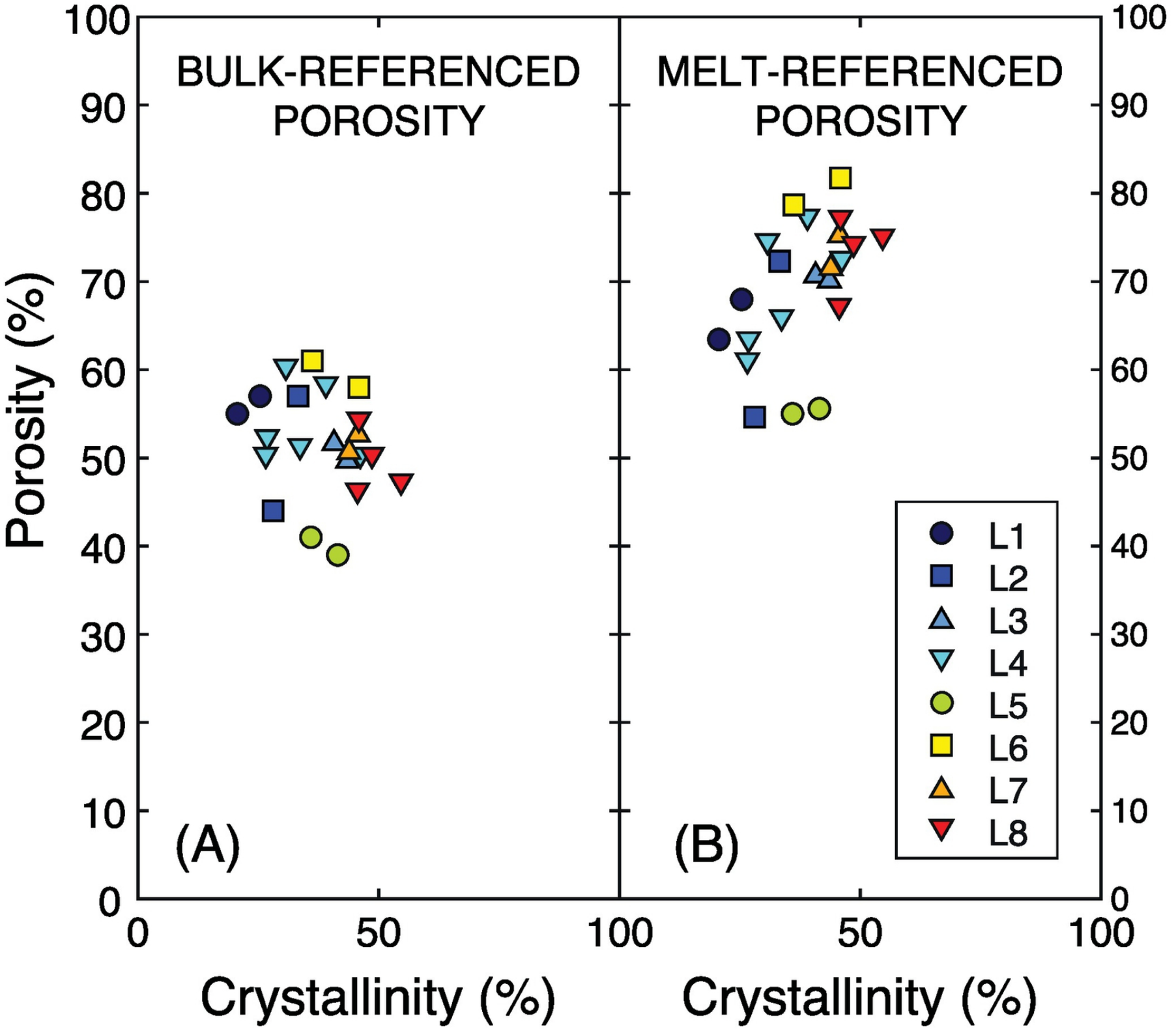
BULK-REFERENCED POROSITY
MELT-REFERENCED POROSITY
Porosity (%)
Crystallinity (%)
Crystallinity (%)
(A)
(B)
L1
L2
L3
L4
L5
L6
L7
L8
0
10
20
30
40
50
60
70
80
90
100
0
50
100

Figure 9

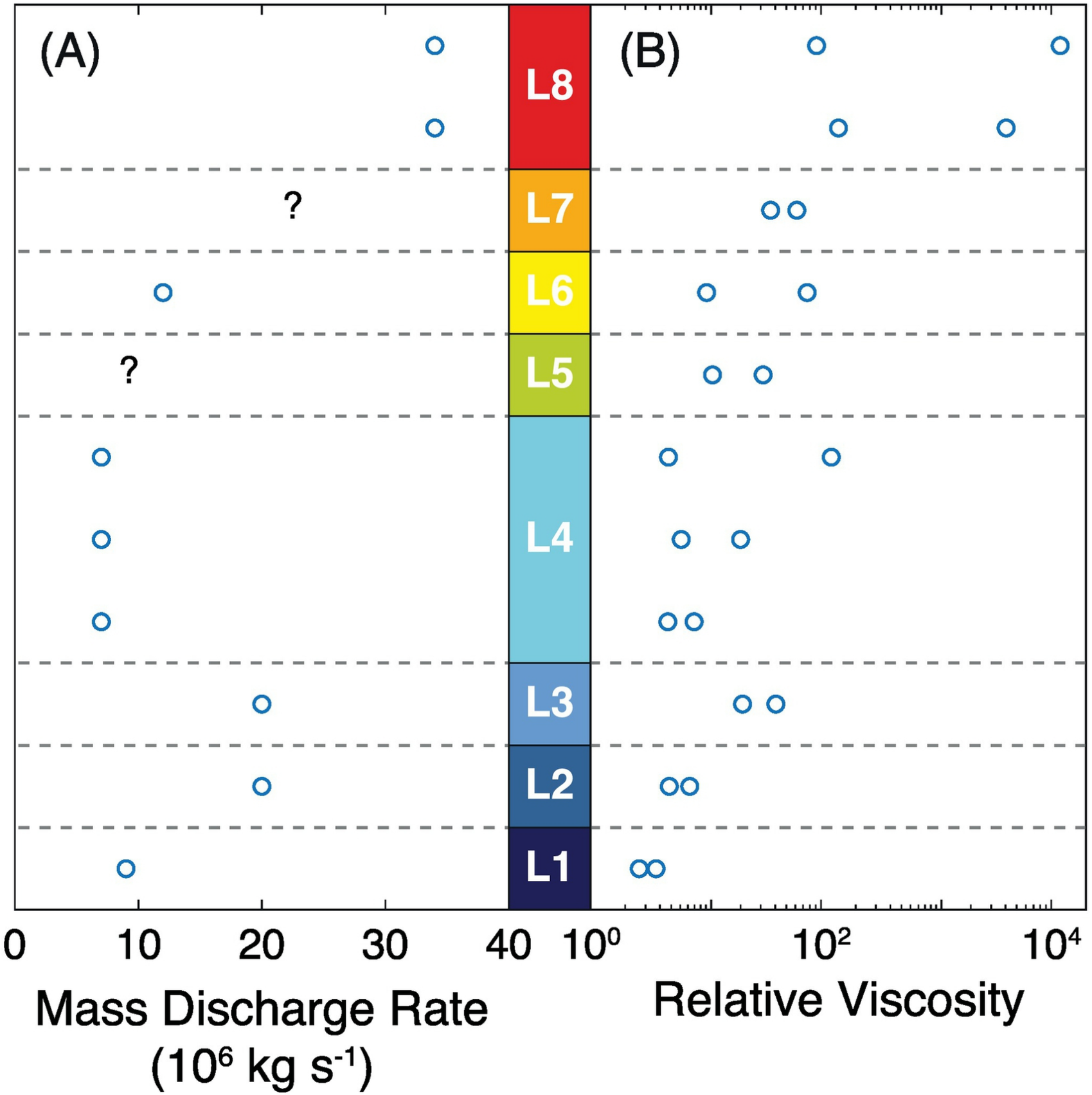
(A)
(B)
L8
L7
L6
L5
L4
L3
L2
L1
?
?
0
10
20
30
40
10^0
10^2
10^4
Mass Discharge Rate
(10^6 kg s^{-1})
Relative Viscosity

Figure 10

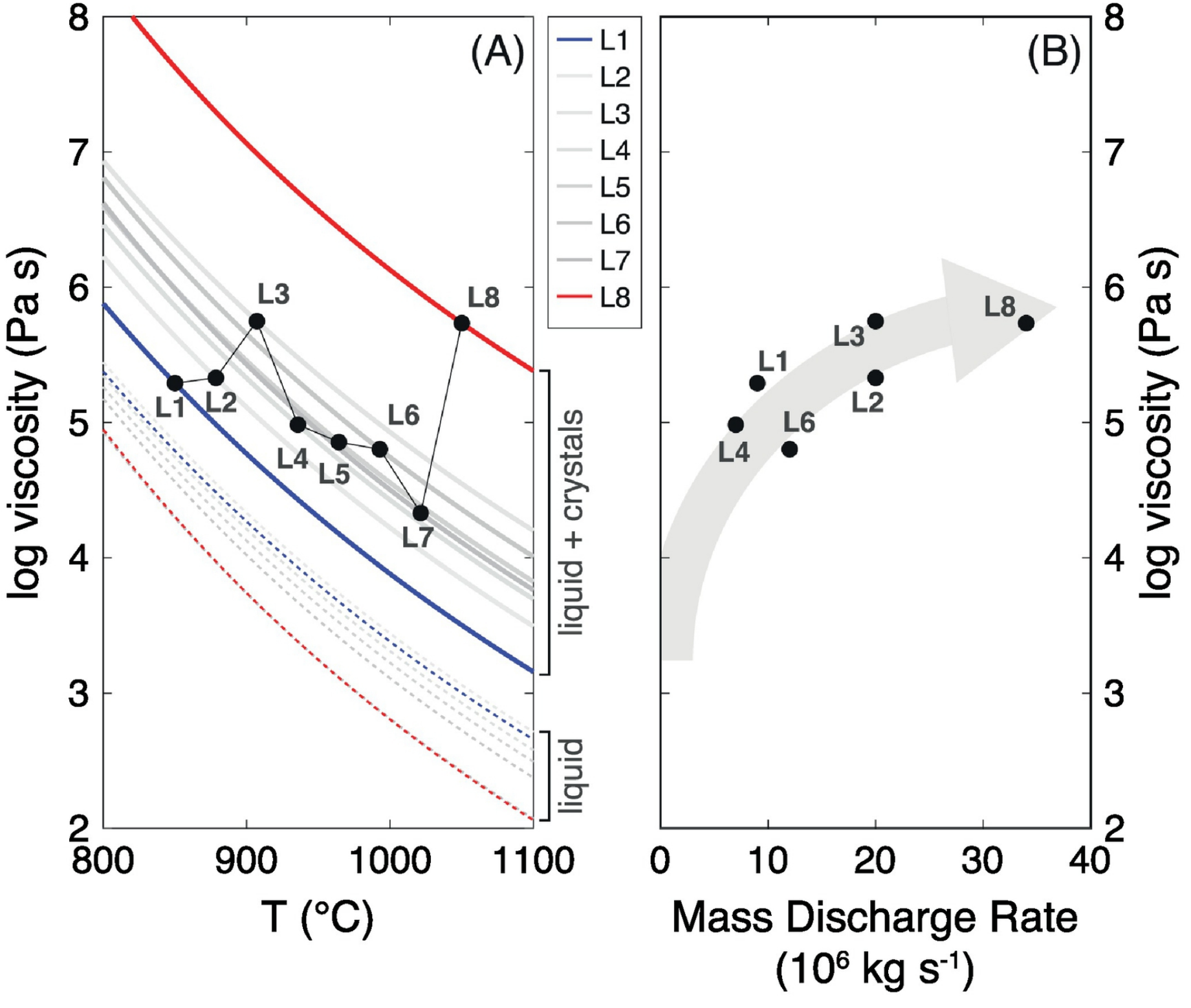
(A)
(B)
L1
L2
L3
L4
L5
L6
L7
L8
liquid + crystals
liquid
log viscosity (Pa s)
T (°C)
Mass Discharge Rate
(10⁶ kg s⁻¹)
800
900
1000
1100
0
10
20
30
40
2
3
4
5
6
7
8

Figure 11

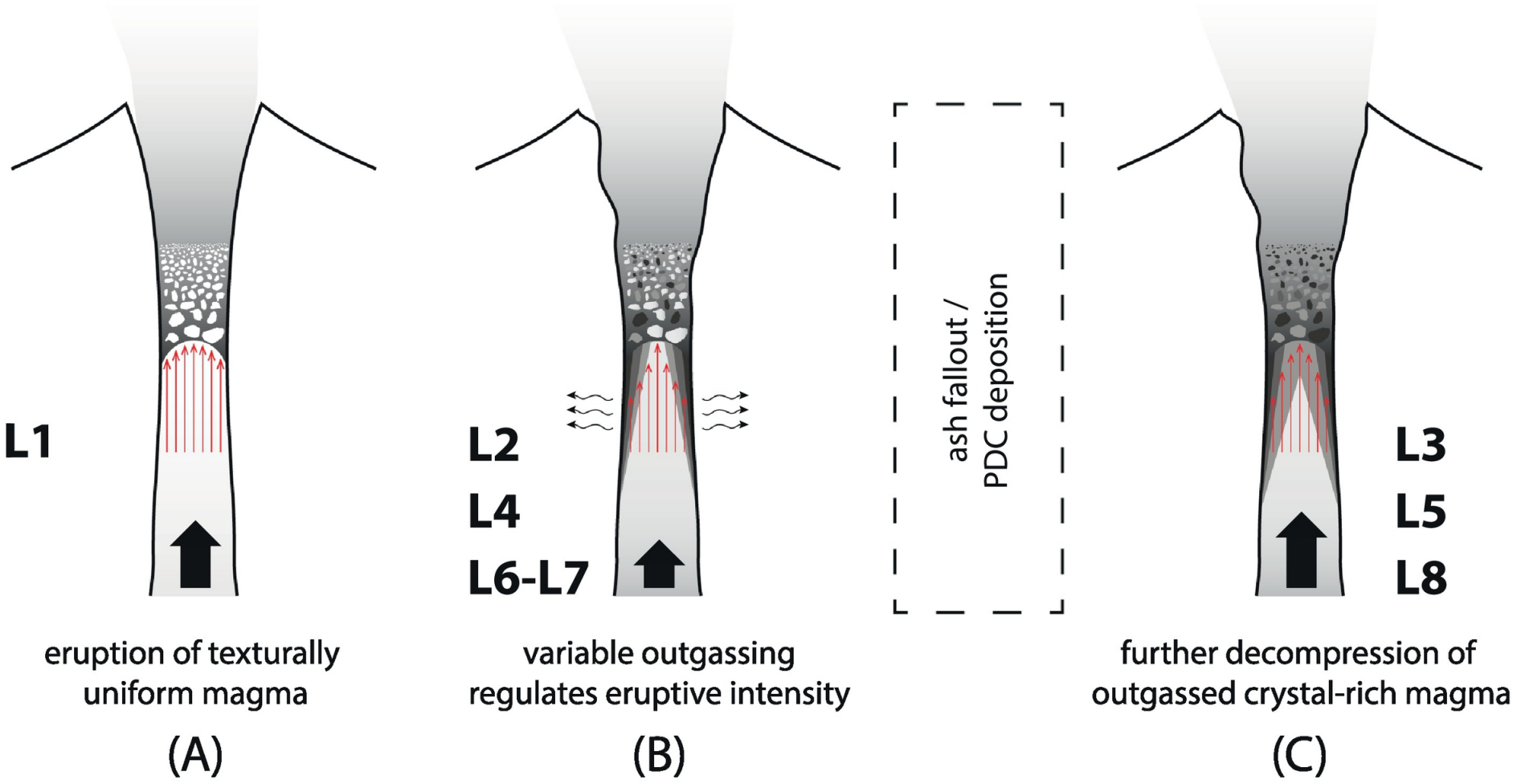
L1
L2
L4
L6-L7
ash fallout /
PDC deposition
L3
L5
L8
eruption of texturally uniform magma
(A)
variable outgassing regulates eruptive intensity
(B)
further decompression of outgassed crystal-rich magma
(C)

Figure 12